

U.S.N.A. – Trident Scholar project report; no. 365 (2008)

STRUCTURE OF QUASAR CONTINUUM EMISSION REGIONS
AND COSMOLOGY FROM OPTICAL AND X-RAY MICROLENSING
IN GRAVITATIONALLY LENSED QUASARS

by

Midshipman 1/c Michael E. Eyler
United States Naval Academy
Annapolis, Maryland

Certification of Adviser Approval

LCDR Christopher W. Morgan
Physics Department

Acceptance for the Trident Scholar Committee

Professor Joyce E. Shade
Deputy Director of Research & Scholarship

REPORT DOCUMENTATION PAGE			Form Approved OMB No. 074-0188	
Public reporting burden for this collection of information is estimated to average 1 hour per response, including g the time for reviewing instructions, searching existing data sources, gathering and maintaining the data needed, and completing and reviewing the collection of information. Send comments regarding this burden estimate or any other aspect of the collection of information, including suggestions for reducing this burden to Washington Headquarters Services, Directorate for Information Operations and Reports, 1215 Jefferson Davis Highway, Suite 1204, Arlington, VA 22202-4302, and to the Office of Management and Budget, Paperwork Reduction Project (0704-0188), Washington, DC 20503.				
1. AGENCY USE ONLY (Leave blank)		2. REPORT DATE 2 May 2008		3. REPORT TYPE AND DATE COVERED
4. TITLE AND SUBTITLE Structure of Quasar Continuum Emission Regions and Cosmology from Optical and X-ray Microlensing in Gravitationally Lensed Quasars			5. FUNDING NUMBERS	
6. AUTHOR(S) Eyler, Michael E.				
7. PERFORMING ORGANIZATION NAME(S) AND ADDRESS(ES)			8. PERFORMING ORGANIZATION REPORT NUMBER	
9. SPONSORING/MONITORING AGENCY NAME(S) AND ADDRESS(ES)			10. SPONSORING/MONITORING AGENCY REPORT NUMBER	
US Naval Academy Annapolis, MD 21402			Trident Scholar project report no. 365 (2008)	
11. SUPPLEMENTARY NOTES				
12a. DISTRIBUTION/AVAILABILITY STATEMENT This document has been approved for public release; its distribution is UNLIMITED.				12b. DISTRIBUTION CODE
13. ABSTRACT Quasars are the most energetic objects in the universe. They are thought to be powered by the accretion of gas onto super-massive black holes at the centers of galaxies. The structure of these exotic objects is poorly understood because their central engines cannot be resolved with ordinary telescopes. Gravitational telescopes, however, provide the necessary resolution to study the structure of quasar central engines. This project analyzed the microlensing variability in five gravitationally lensed quasar systems to probe the structure of the continuum emission regions at optical and X-ray wavelengths and make time delay estimates in the systems in which sufficient data were available. The flux of each component of the multiply-imaged quasars was measured in many seasons of ground-based optical imagery. Lightcurves were constructed from the flux measurements, and Monte Carlo methods were used to analyze the microlensing variability in the lightcurves. The results of the Monte Carlo routine were analyzed with Bayesian methods, yielding estimates of the time delays and the sizes of the quasar accretion disks in QJ0158-4325 and HE1104-1805. The time delay analysis in QJ0158-4325 was unsuccessful, but an optical accretion disk size estimate of $\log[(rs/cm) \sqrt{\cos i/0.5}] = 14.9 \pm 0.3$ at a rest-frame wavelength of $0.3\mu m$ was possible nonetheless. In HE1104-1805, a time delay of $\Delta t_{AB} = t_A - t_B = 162.2+6.3 -5.9 (1\sigma)$ and an accretion disk size of $\log[(rs/cm) \sqrt{\cos i/0.5}] = 15.7+0.4 -0.5$ at $0.2 \mu m$ were estimated. The optical accretion disk sizes of both systems are consistent with thin accretion disk theory and confirm the recently established quasar accretion disk size-black hole mass relation. (cont on p.2)				
14. SUBJECT TERMS cosmology: observations — accretion, accretion disks — dark matter — gravitational lensing — quasars: general			15. NUMBER OF PAGES 42	
			16. PRICE CODE	
17. SECURITY CLASSIFICATION OF REPORT	18. SECURITY CLASSIFICATION OF THIS PAGE	19. SECURITY CLASSIFICATION OF ABSTRACT	20. LIMITATION OF ABSTRACT	

ABSTRACT

Quasars are the most energetic objects in the universe. They are thought to be powered by the accretion of gas onto super-massive black holes at the centers of galaxies. The structure of these exotic objects is poorly understood because their central engines cannot be resolved with ordinary telescopes. Gravitational telescopes, however, provide the necessary resolution to study the structure of quasar central engines. This project analyzed the microlensing variability in five gravitationally lensed quasar systems to probe the structure of the continuum emission regions at optical and X-ray wavelengths and make time delay estimates in the systems in which sufficient data were available.

The flux of each component of the multiply-imaged quasars was measured in many seasons of ground-based optical imagery. Lightcurves were constructed from the flux measurements, and Monte Carlo methods were used to analyze the microlensing variability in the lightcurves. The results of the Monte Carlo routine were analyzed with Bayesian methods, yielding estimates of the time delays and the sizes of the quasar accretion disks in QJ0158–4325 and HE1104–1805. The time delay analysis in QJ0158–4325 was unsuccessful, but an optical accretion disk size estimate of $\log[(r_s/\text{cm})\sqrt{\cos i/0.5}] = 14.9 \pm 0.3$ at a rest-frame wavelength of $0.3\mu\text{m}$ was possible nonetheless. In HE1104–1805, a time delay of $\Delta t_{AB} = t_A - t_B = 162.2^{+6.3}_{-5.9}$ (1σ) and an accretion disk size of $\log[(r_s/\text{cm})\sqrt{\cos i/0.5}] = 15.7^{+0.4}_{-0.5}$ at $0.2\mu\text{m}$ were estimated. The optical accretion disk sizes of both systems are consistent with thin accretion disk theory and confirm the recently established quasar accretion disk size–black hole mass relation.

With motivation to test for a similar correlation at X-ray wavelengths, simultaneous optical and X-ray accretion disk size estimates were attempted for the systems B1422+0231, RXJ0911+0551, and HE0230–2130. For RXJ0911+0551, the analysis successfully yielded an optical accretion disk size estimate of $\log[(r_s/\text{cm})\sqrt{\cos i/0.5}] = 16.1^{+0.4}_{-0.5}$ at $0.2\mu\text{m}$. For B1422+0231 and HE0230–2130, however, the sparseness of the optical monitoring data prevented accretion disk size estimates. Nonetheless, the analysis yielded X-ray size estimates of $\log[R_{1/2,\text{X}}/\text{cm}] = 15.4 \pm 0.7$, $\log[R_{1/2,\text{X}}/\text{cm}] = 15.7^{+0.6}_{-0.7}$, and $\log[R_{1/2,\text{X}}/\text{cm}] = 15.0^{+0.7}_{-0.8}$ for HE0230–2130, B1422+0231, and RXJ0911+0551, respectively. When combined with recently published X-ray size estimates in two other quasars, it was found that X-ray size is related to black hole mass by $\log[r_{1/2,\text{X}}/\text{cm}] = (15.2 \pm 0.2) + (0.74 \pm 0.28) \log[M_{\text{BH}}/10^9 M_\odot]$. The size estimates are close to the innermost stable circular orbits, favoring X-ray emission models with X-ray continuum emission within several gravitational radii of the central black hole.

Subject headings: cosmology: observations — accretion, accretion disks — dark matter — gravitational lensing — quasars: general

ACKNOWLEDGEMENTS

Many thanks to LCDR C. W. Morgan, whose effort, generosity, and patience made this research possible and rewarding. Thanks also to Professors C. S. Kochanek, B. W. Peterson, and many others at The Ohio State University for hosting a summer internship and offering their personal assistance in the early phases of this project.

Many thanks to the U.S. Naval Academy Trident Scholar and Bowman Scholar Programs and the Office of Naval Research for providing the opportunity and funding to conduct this research during both a summer internship and the academic year. Thanks also to faculty in the USNA Physics Department for their support and input.

This work is based on observations obtained with the Small and Moderate Aperture Research Telescope System (SMARTS) 1.3m, which is operated by the SMARTS Consortium; observations obtained by collaborators on the 1.2m Leonard Euler Swiss Telescope; publicly available archival data of the *Chandra X-Ray Observatory* obtained through the Chandra X-Ray Observatory Center, which is operated by the Smithsonian Astrophysical Observatory for and on behalf of the National Aeronautics Space Administration under contract NAS 8-03060; and imaging performed using the NASA/ESA *Hubble Space Telescope* for program HST-GO-9744 of the Space Telescope Science Institute, which is operated by the Association of Universities for Research in Astronomy, Inc., under NASA contract NAS 5-26666. This research also made extensive use of a Beowulf computer cluster obtained through the Cluster Ohio program of the Ohio Supercomputer Center.

Contents

1	Introduction	4
1.1	Quasars	4
1.2	Gravitational Lensing of Quasars	6
1.3	Summary	10
2	Observations and Data Reduction	10
2.1	HST Observations and Photometric Models	10
2.2	Optical Monitoring	13
2.3	X-ray Observations	15
3	Data Analysis	15
3.1	<i>HST</i> Images and Mass Models	15
3.2	Microlensing Analysis Technique	17
3.3	Time Delay Analysis of QJ0158–4325 and HE1104–1805	20
3.4	Joint X-Ray/Optical Analysis of HE0230–2130, B1422+0231, and RXJ0911+0551	22
4	Results	23
4.1	HE1104–1805	23
4.2	QJ0158–4325	24
4.3	X-ray Fitting Results	25
4.4	Discussion	28
5	Conclusions	31
	References	32
	Appendix A: Monitoring Data	34
	Appendix B: Glossary	40

1. Introduction

1.1. Quasars

1.1.1. Overview

Quasars are the brightest and most distant objects in the known universe. Thanks to large-scale surveys such as the Sloan Digital Sky Survey and the Two-Degree Field Survey, more than 10^5 quasars have been positively identified. They are the most luminous of a class of objects known as active galactic nuclei, which lie at the cores of young, evolving galaxies in the early universe. Quasars are extremely energetic, with typical luminosities ~ 100 times that of the Milky Way galaxy.

Originally named “quasi-stellar objects” due to their point-like appearance, quasars have distinctly non-stellar, flat spectra with some prominent broad-line emission. They undergo dramatic non-periodic variations in luminosity in every waveband, with many objects exhibiting variability of 0.3 - 0.5 **magnitudes**¹ on time scales of months, and a few on time scales of only days (e.g., Peterson, 1997). The time scale for intrinsic variability Δt_{var} implies a maximum size scale $R_{max} \approx c \Delta t_{var}$, so the majority of a quasar’s radiation must come from regions on the order of light days across (1 light day = 2.54×10^{15} cm), roughly the size of the Solar System. Combined with typical magnitude measurements, such size estimates suggest that quasars are uniquely powerful – though they are compact objects, each one radiates with multiple times the luminosity of an entire galaxy.

1.1.2. Structure of Quasars

Since quasars exist only at cosmological distances, no conventional telescopes are capable of resolving their impossibly small angular size ($\sim \mu\text{arcsec}$). This is particularly problematic in studying quasars’ innermost regions, from which the continuum portion of the quasar spectrum is thought to originate. Nearly all that is currently known about quasar continuum emission regions has been inferred from their spectral energy distributions or the timescale of their variability. Based on these properties, quasars are thought to be powered by a disk of hot gas accreting onto a central supermassive black hole. Their spectacular energy output is generated as the infalling gas becomes heated in a dissipative accretion disk. In a simple accretion disk model, the disk radiates locally as a blackbody, with a radial temperature profile of

$$T(R)^4 = \frac{3GM_{\text{BH}}\dot{M}}{8\pi R^3\sigma} \left[1 - \left(\frac{R_{\text{in}}}{R} \right)^{1/2} \right], \quad (1)$$

¹See the glossary in Appendix B for further explanation of the magnitude scale. Throughout this report, terms explained in the glossary will be printed in bold where they first appear in the text.

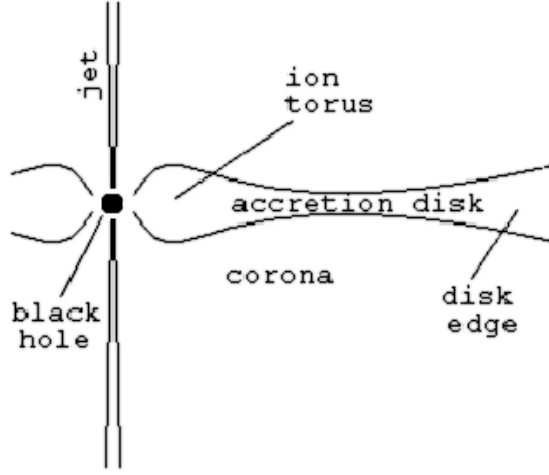


Fig. 1.— A cross-sectional diagram (not to scale) of the model of a quasar central engine.

where G is the universal gravitational constant, M_{BH} is the mass of the central black hole, \dot{M} is the rate of mass accretion, σ is the Stefan-Boltzmann constant, and R_{in} is the inner edge of the disk set by the **innermost stable circular orbit** around the black hole (Shakura & Sunyaev, 1973). Other structures in the standard model include magnetically generated jets of charged particles flowing outward along the disk axis, a hot corona around the disk, and an “ion torus” in the inner disk regions that arises when accretion rates are sufficiently low. Such torii are a possible mechanism for helping to produce the jets (Peterson, 1997). A diagram of these components is shown in Figure 1.

Although a significant fraction of quasars’ **bolometric luminosity** is emitted in X-rays (Elvis et al., 1994), the structure of their X-ray emission regions is poorly understood. Few current accretion disk models produce X-rays at all, and those that do emit X-rays produce them on a wide range of size scales relative to the black hole’s gravitational radius $r_g = GM_{\text{BH}}/c^2$. The present dominant emission model produces X-rays via **inverse Compton scattering** in a hot, extended corona that extends over much of the accretion disk (e.g., Haardt & Maraschi, 1991; Merloni, 2003). Hawley & Balbus (2002) also predict a large X-ray emission region, but in their model, a hot gas jet drags across the cooler accretion disk, resulting in **bremsstrahlung**. The X-ray emission comes primarily from an inner torus with radius $r \lesssim 20r_g$, but the continuum emission region extends out to $r \simeq 200r_g$. In contrast, the relativistic magnetohydrodynamic model of Hirose et al. (2004) predicts a current-carrying inner torus of radius $r \lesssim 10r_g$ that is able to emit a moderate amount of X-rays. The emission scale is even smaller in the “lamp-post” (Martocchia et al., 2002) and “aborted jet” (Ghisellini et al., 2004) models, which both predict emission structures with sizes $r \lesssim 3.0r_g$. Because quasar continuum emission regions cannot be resolved with conventional telescopes, the X-ray continuum emission structure remains uncertain.

1.2. Gravitational Lensing of Quasars

1.2.1. Macrolensing

Gravitational lensing occurs when a foreground mass (the “lens”) and background light source are in alignment or near-alignment along an observer’s line of sight. In such a configuration, the gravitational potential of the lens deflects the light rays coming from the source. In the case of a point source perfectly aligned behind a spherically symmetric mass M along the line of sight, the light from the source is bent so that it appears as a circular ring around the lensing mass. This ring has an angular “Einstein radius” of

$$\theta_E = \sqrt{\frac{4GM}{c^2} \frac{D_{\text{LS}}}{D_{\text{OL}}D_{\text{OS}}}}, \quad (2)$$

where D_{OL} , D_{OS} , and D_{LS} are **angular diameter distances** from the observer to the lens, from the observer to the source, and from the lens to the source, respectively.

If the source and the lensing mass are slightly misaligned, two distorted images of the source will appear to the observer. The image positions and distortions are a function of the lens mass and the relative positions of the source, lens, and observer (Refsdal, 1964). The simple point source–spherical mass scenario most closely models the lensing of light from a point-like source (e.g., a star) by a compact foreground mass such as a star or planet.

In ~ 100 of the 10^5 known quasars, a foreground galaxy falls along the line of sight, but the lensing geometry is significantly more complicated than in the symmetric point source–spherical mass case. The mass in lens galaxies is extended and roughly elliptical in its distribution, leading to one, three, or five images depending on the source position, with the central image being very faint (Blandford et al., 1989). More complex lensing potentials can lead to arbitrary numbers of images, but in most lensed quasar systems, two or four images are observed. Figure 2 illustrates the geometry of a double-image system.

The photons forming each image take different paths through intergalactic space and the gravitational potential of the lens galaxy. As a result, the path lengths and amounts of general relativistic time dilation experienced by the photons differ, causing time delays between the appearance of the quasar’s variability in each image.

Because the cosmological distances separating the quasar, lens galaxy, and observer are large compared to the size of the lens galaxy, multiple imaging and time delays can both be treated with the thin-lens approximation of geometric optics. In this treatment, presented in Kochanek & Schechter (2004), the most general mathematical expression for the light travel time is

$$\tau(\vec{x}) = \left[\frac{1+z_l}{c} \right] \left[\frac{D_{\text{OL}}D_{\text{OS}}}{D_{\text{LS}}} \right] \left[\frac{1}{2}(\vec{x} - \vec{\beta})^2 - \psi(\vec{x}) \right], \quad (3)$$

where z_l is the lens **redshift** and \vec{x} and $\vec{\beta}$ are the angular positions of the image and the source, respectively. The term $\psi(\vec{x})$ (discussed below) accounts for the gravitational

component of the light travel time. The term $\frac{1}{2}(\vec{x} - \vec{\beta})^2$ is the geometric component that accounts for the light travel path length in the small-angle approximation.

Equation 3 is written in a two-dimensional coordinate system that represents the projection of the source, images, and lens galaxy onto the plane of the sky. In particular, the term $\psi(\vec{x}) = (2/c^2)(D_{LS}/D_{OS}) \int \phi dz$ is a two-dimensional gravitational potential for the lens obtained by integrating the three-dimensional lensing potential ϕ along the line of sight. This two-dimensional potential is related to the local surface density κ of the lens galaxy by the Poisson equation $\nabla^2 \phi(\vec{x}) = 2\kappa(\vec{x})$. Here, $\kappa = \Sigma/\Sigma_{crit}$ is dimensionless; it is written in units of the critical surface density for gravitational lensing

$$\Sigma_{crit} = \frac{c^2 D_{OS}}{4\pi G D_{OL} D_{LS}}, \quad (4)$$

a convenient quantity that corresponds to the surface density obtained by “smearing” the lens mass uniformly in the circle enclosed by the lens Einstein radius.

Given a lens galaxy gravitational potential ψ , the image positions can be determined using equation 3. If light travel time is plotted as a function of image position, then by

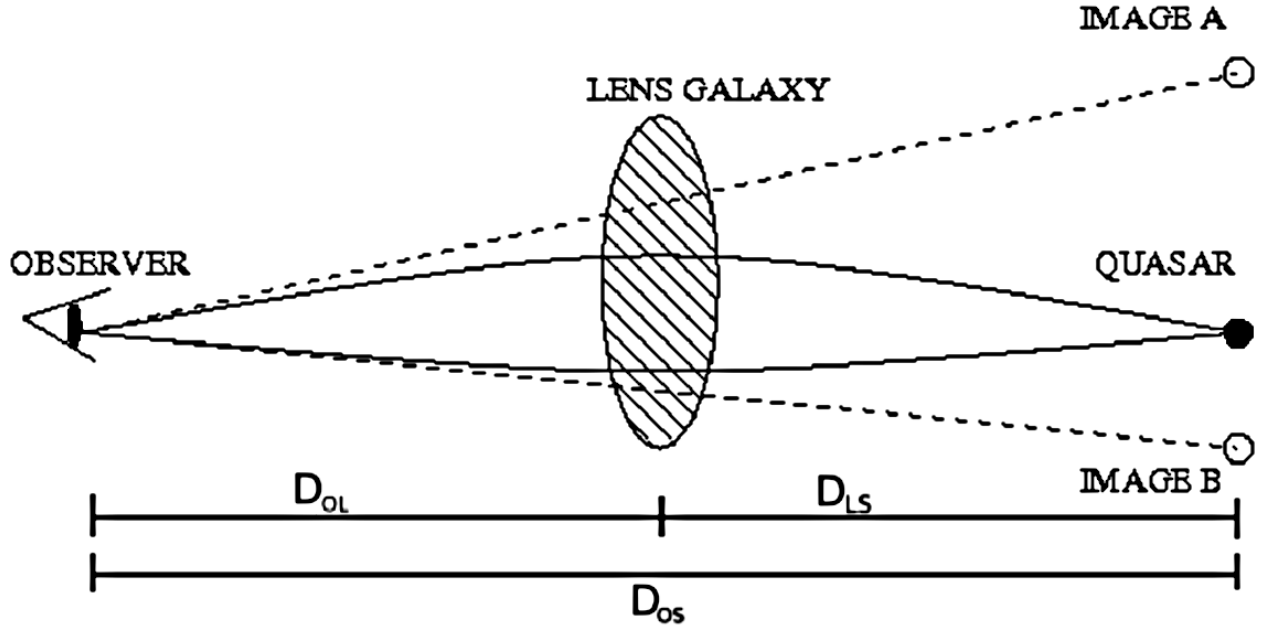


Fig. 2.— A simplified diagram illustrating the formation of multiple images by a lens galaxy. Common configurations of lens systems produce two images. Note that the diagram is not to scale, though an attempt has been made to illustrate that the light from the quasar passes through the disk of the lens galaxy and that the galaxy is not perfectly aligned with the line of sight. The relevant angular diameter distances are labeled.

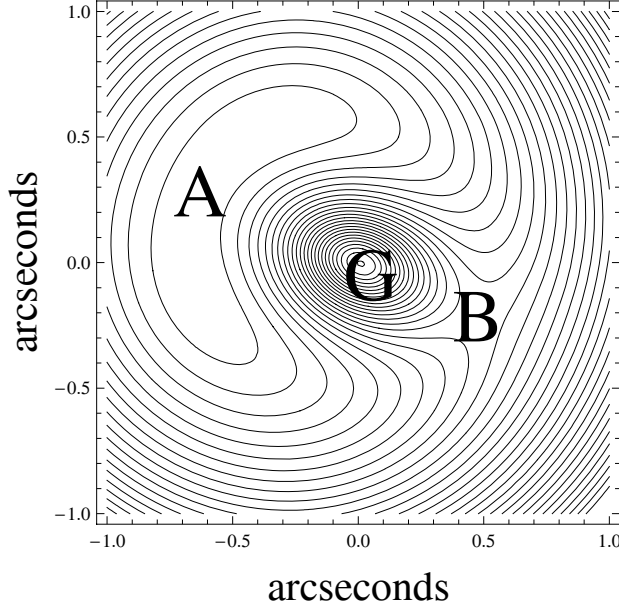


Fig. 3.— A contour plot of the time delay surface for QJ0158–4325. Image A appears at a minimum and B at a saddle point. The center of the lens galaxy is marked G.

Fermat’s principle, images will appear at stationary points in the resulting time delay surface (where $\vec{\nabla}\tau = 0$), as shown in Figure 3. Taking the gradient of equation 3 at those points yields the expression

$$\vec{\beta} = \vec{x} - \vec{\nabla}\psi(\vec{x}), \quad (5)$$

relating the source position $\vec{\beta}$ to the image position \vec{x} by a deflection angle $\vec{\alpha} = \vec{\nabla}\psi$. Thus, the image positions are determined entirely by the terms in equation 3 – the lens gravitational potential and the relative source and lens positions in the plane of the sky. Further manipulation yields the dependence of the deflection angle on the surface mass density and the distortion and magnification of the images as a function of position.

1.2.2. Microlensing

Intrinsic source variability is one of two contributors to the variability in lensed quasar images. The other is gravitational microlensing by stars and other compact objects in the foreground galaxy. “Microlensing” is the term used to describe cases of lensing in which the angular separation of the images is too small to permit resolution by the observer. Recall that the spatial scale for the lensing is set by the lens Einstein radius (θ_E), where $\theta_E \sim \sqrt{MD_{LS}/D_{OL}D_{OS}}$. Therefore, if the lensing mass is sufficiently small and the distances to the lens and source are sufficiently large, the lensed images will be unresolved and appear to the observer as a single aggregate image (Wambsganss, 2006). One regime in which this commonly occurs is the lensing of quasar light by the stars in lens galaxies, because the

stellar masses are small and the cosmological distances involved are very large.

Although the lensed images are unresolvable, the microlensing is still observable as a magnification of the original source flux. This effect occurs because surface brightness (flux per unit solid angle) is always conserved, and the lensed images cover more solid angle than the original source. As a result, the flux of the aggregate image is magnified from that of the original (Blandford et al., 1989).

The positions and distortions of the “micro-images” change with time due to the relative motions of the source, observer, and lens. This causes time-varying magnification of the aggregate image fluxes – microlensing “events.” Given the multitude of stars in the two-dimensional projection of a typical lens galaxy, quasar microlensing events occur frequently. However, the superposition of the gravitational potentials of many stars in the vicinity of the quasar images results in complicated magnification patterns. The variability, which occurs on typical timescales of weeks or years, is consequently very complex (Kochanek, 2004). So, rather than attempting to analyze single high-magnification events, this project used a statistical approach to analyze long-term monitoring data that contained many microlensing events.

The microlensing variability is superimposed on the quasar’s intrinsic variability, which can complicate the analysis of the microlensing signal and the estimation of time delays. Fortunately, the two types of variability can be separated. Whereas the intrinsic variability is correlated because it arises from a single source, the microlensing variability is uncorrelated because each image’s photons pass through a different part of the lens galaxy. This fact can be exploited in microlensing analysis (see §3.3). Additionally, microlensing events often occur on timescales longer than that of the intrinsic variability, which is helpful when attempting a time delay estimate (Eigenbrod et al., 2005).

Microlensing may interfere with time delay estimates, but when it can be modeled well, analysis of the microlensing variability in lensed quasar images can yield estimates of the size and structure of quasar accretion disks (Kochanek, 2004). For QJ0158–4325, the Einstein radius of a lens galaxy star is given by

$$\theta_E = \sqrt{\frac{4GM}{c^2} \frac{D_{LS}}{D_{OL}D_{OS}}} = 4.3 \left(\frac{M}{M_\odot} \right)^{1/2} \mu\text{arcsec}, \quad (6)$$

which, when projected onto the plane of the quasar (the “source plane”), translates to a physical scale of

$$R_E = D_{OS}\theta_E = 7.8 \times 10^{16} \left(\frac{M}{M_\odot} \right)^{1/2} \text{ cm}. \quad (7)$$

The Einstein radii are similar enough in scale to the continuum emission region sizes that the amount of microlensing variability is sensitive to the source size. Also, since the Einstein radius sets the characteristic scale over which microlensing occurs (Wyithe & Turner, 2001) and the Einstein radii for the lens galaxy stellar masses are small, the crossing times for microlensing events are short enough that events are observable. Microlensing is therefore a unique tool for probing continuum emission region sizes.

1.3. Summary

The observations are described in §2. The microlensing analysis is described in §3, the results are presented and discussed in §4, and the conclusions are summarized in §5. This analysis assumed a flat concordance cosmology with mass density $\Omega_0 = 0.3$, energy density $\Lambda_0 = 0.7$, and **Hubble constant** $H_0 = 70 \text{ km s}^{-1} \text{ Mpc}^{-1}$ (see Peebles, 1993).

2. Observations and Data Reduction

There were three components to the data in this investigation. High-resolution *Hubble Space Telescope* (*HST*) imaging was used to measure the precise **astrometry** of the quasar images, lens galaxy, and quasar host galaxy in each system. Several seasons of ground-based optical monitoring were used to construct the lightcurves for each image in each lensed quasar. Finally, several epochs of X-ray imagery from the *Chandra X-Ray Observatory* (*Chandra*) were used to create sparse X-ray “lightcurves” in three of the five systems.

2.1. HST Observations and Photometric Models

Precise astrometry and **photometry** were needed to generate a series of macroscopic mass models for each system (see §3.2). *HST* images were chosen for this purpose because space telescope resolution is limited by diffraction rather than atmospheric conditions. *HST* imagery in the *V*- (F555W), *I*- (F814W), and *H*- (F160W) bands was used (with the exception of HE0230–2130, which was imaged only in the *V*- and *I*-bands).² The images, displayed in Figure 4, were taken by the CfA-Arizona Space Telescope LEns Survey (CASTLES; see Falco et al., 2001). The astrometry and photometry were measured with the *imfitfits* software package (see Lehár et al., 2000; Falco et al., 2001). The quasar images were modeled as point sources, the lens galaxies using the **de Vaucouleurs profile**, and the quasar host galaxies as lensed exponential disks. The astrometry and photometry are presented in Table 1.

²For a discussion of *HST* filters, see the filter descriptions for the NICMOS and WFPC2 instruments on the Space Telescope Science Institute website (<http://www.stsci.edu/hst>).

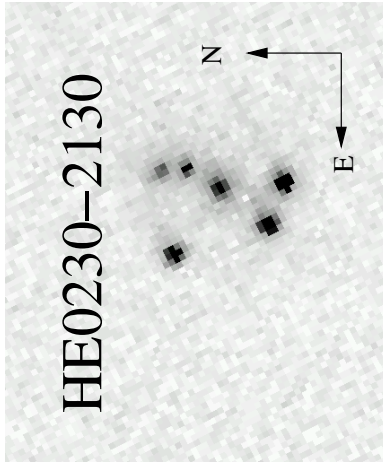
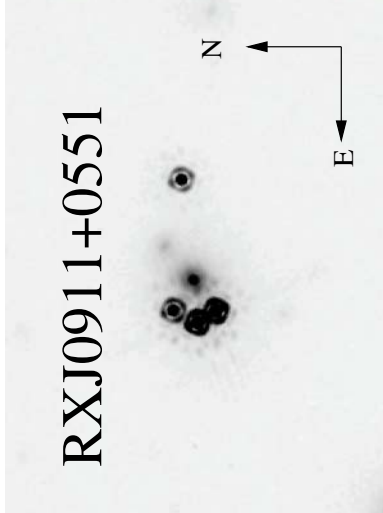
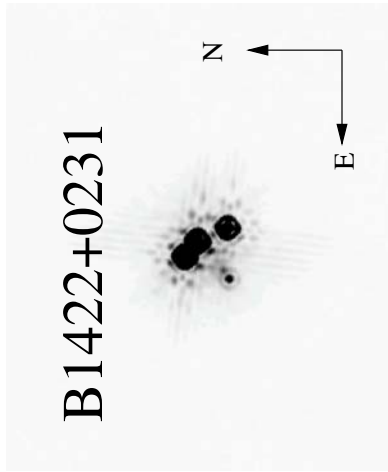
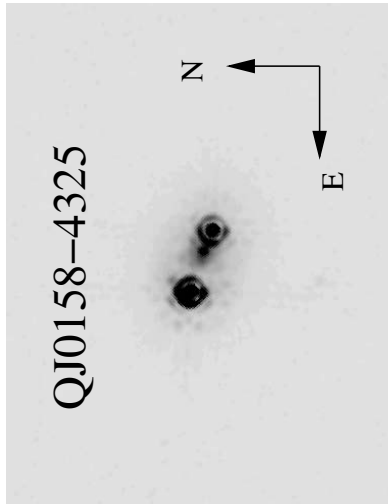
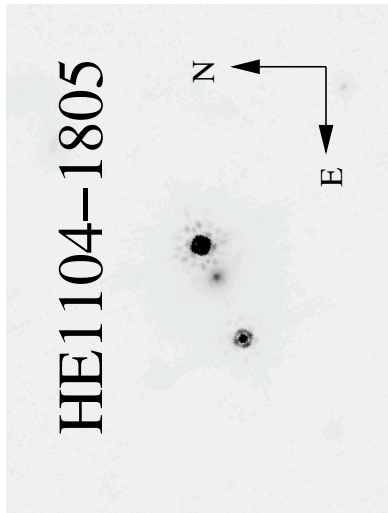


Fig. 4.— *HST* images of QJ0158–4325, HE1104–1805, HE0230–2130, B1422+0231, and RXJ0911+0551 from the CASTLES survey. The HE0230–2130 image was taken in the *I*-band using the WFP/C2 instrument, and the others are *H*-band images taken using the NICMOS instrument. The quasar images and lens galaxies (particularly their centers) are visible. Two systems (HE0230–2130 and B1422+0231) have multiple lens galaxies.

Lens	Component	Astrometry		Photometry	
		ΔR_A	ΔDec	H=F160W	I=F814W
QJ0158-4325	A	$\equiv 0$	$\equiv 0$	16.47 ± 0.03	17.81 ± 0.04
	B	$-1''.156 \pm 0''.003$	$-0''.398 \pm 0''.003$	17.27 ± 0.03	18.62 ± 0.11
	G	$-0''.780 \pm 0''.016$	$-0''.234 \pm 0''.006$	16.67 ± 0.13	18.91 ± 0.17
HE1104-1805	A	$\equiv 0$	$\equiv 0$	15.91 ± 0.01	16.40 ± 0.03
	B	$+2''.901 \pm 0''.003$	$-1''.332 \pm 0''.003$	17.35 ± 0.03	17.95 ± 0.04
	G	$+0''.965 \pm 0''.003$	$-0''.500 \pm 0''.003$	17.52 ± 0.09	20.01 ± 0.10
HE0230-2130	A	$\equiv 0$	$\equiv 0$		19.02 ± 0.09
	B	$+0''.698 \pm 0''.003$	$+0''.256 \pm 0''.003$	–	19.22 ± 0.07
	C	$+1''.198 \pm 0''.005$	$+1''.828 \pm 0''.003$	–	19.59 ± 0.09
	D	$-0''.244 \pm 0''.007$	$+1''.624 \pm 0''.007$	–	21.21 ± 0.11
	G	$+0''.072 \pm 0''.003$	$+1''.085 \pm 0''.005$	–	20.39 ± 0.43
	G'	$-0''.212 \pm 0''.025$	$+2''.059 \pm 0''.016$	–	20.34 ± 0.41
					19.58 ± 0.12
B1422+0231	A	$+0''.385 \pm 0''.000$	$+0''.317 \pm 0''.000$	14.41 ± 0.02	15.88 ± 0.01
	B	$\equiv 0$	$\equiv 0$	14.29 ± 0.03	15.85 ± 0.01
	C	$-0''.336 \pm 0''.003$	$-0''.750 \pm 0''.003$	14.98 ± 0.03	17.09 ± 0.03
	D	$+0''.948 \pm 0''.004$	$-0''.802 \pm 0''.003$	18.14 ± 0.02	20.44 ± 0.05
	G	$+0''.742 \pm 0''.003$	$-0''.656 \pm 0''.004$	17.57 ± 0.01	21.80 ± 0.05
					19.66 ± 0.06
B1422+0231	A	$\equiv 0$	$\equiv 0$	17.59 ± 0.02	18.83 ± 0.04
	B	$+0''.260 \pm 0''.003$	$+0''.406 \pm 0''.003$	17.65 ± 0.02	19.18 ± 0.03
	C	$-0''.018 \pm 0''.003$	$+0''.960 \pm 0''.003$	18.34 ± 0.03	19.89 ± 0.05
	D	$-2''.972 \pm 0''.003$	$+0''.792 \pm 0''.003$	18.65 ± 0.02	20.27 ± 0.10
	G	$-0''.698 \pm 0''.004$	$+0''.512 \pm 0''.005$	17.93 ± 0.03	22.97 ± 0.19
	G'	$-1''.452 \pm 0''.039$	$+1''.177 \pm 0''.011$	20.61 ± 0.01	25.78 ± 1.07
					22.83 ± 0.27

Note. — A – D are images and G⁽ⁱ⁾ are lens galaxies. ΔR_A and ΔDec are **right ascension** and **declination**.

Table 1. HST Astrometry and Photometry

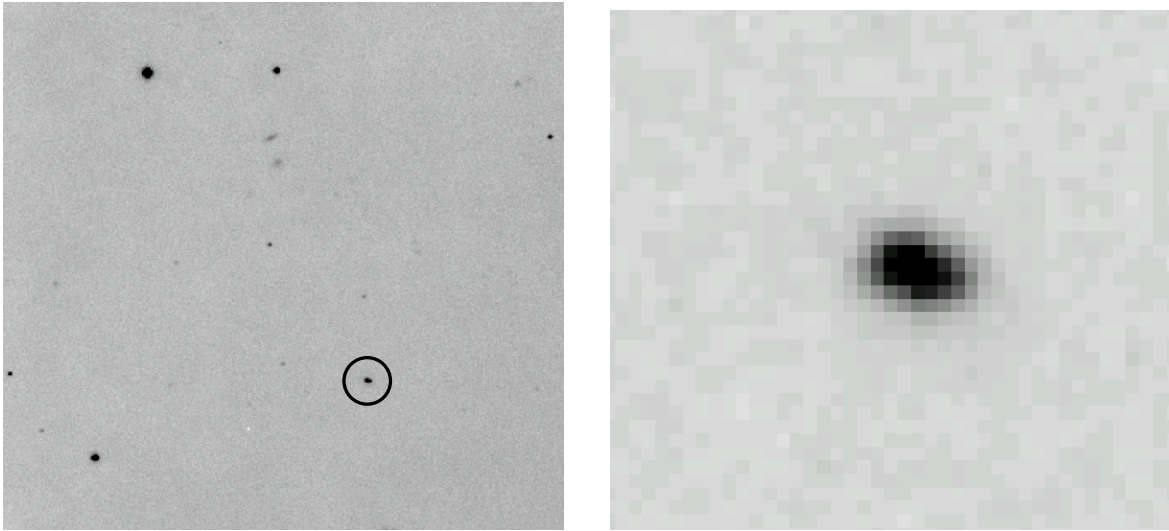


Fig. 5.— An optical ground-based image of QJ0158–4325 taken on 1 February 2007 with the SMARTS 1.3-m telescope. The left frame shows the quasar (circled) and some of the surrounding star field. Several galaxies are visible along with some of the reference stars used to perform the relative photometry. The right frame is a close-up of the quasar that clearly shows the overlap between the two quasar images.

2.2. Optical Monitoring

The five systems were monitored at optical wavelengths with several ground-based telescopes. QJ0158–4325 was observed at fairly regular intervals (approximately 1-2 times weekly) in the *R*-band using the ANDICAM optical-infrared camera (DePoy et al., 2003) on the queue-scheduled SMARTS 1.3m telescope at the Cerro Tololo Inter-American Observatory and using the Leonard Euler 1.2m Swiss telescope at the La Silla Observatory.³ To date, the QJ0158–4325 data spans four seasons. The combined *V*- and *R*-band data used in the HE1104–1805 analysis were taken from Poindexter et al. (2007), and RXJ0911+0551 was observed using the SMARTS telescope. No ground-based optical monitoring data were available for HE0230–2130 or B1422+0231, so the *V*-band *HST* flux measurements were used.

On each night, several 300-second exposures were taken successively. The separate images prevented **CCD saturation** and minimized the loss of data in cases of contamination (e.g., satellite trails or **cosmic ray** hits). These individual images were then summed to maximize the signal-to-noise ratio. Figure 5 shows an example of one night’s data from QJ0158–4325. In this system, data were rejected on nights when **seeing** was 1.7 arcseconds

³The Euler data were obtained by collaboration with C. Vuissoz, F. Courbin, and G. Meylan of the École Polytechnique Fédérale de Lausanne, Switzerland.

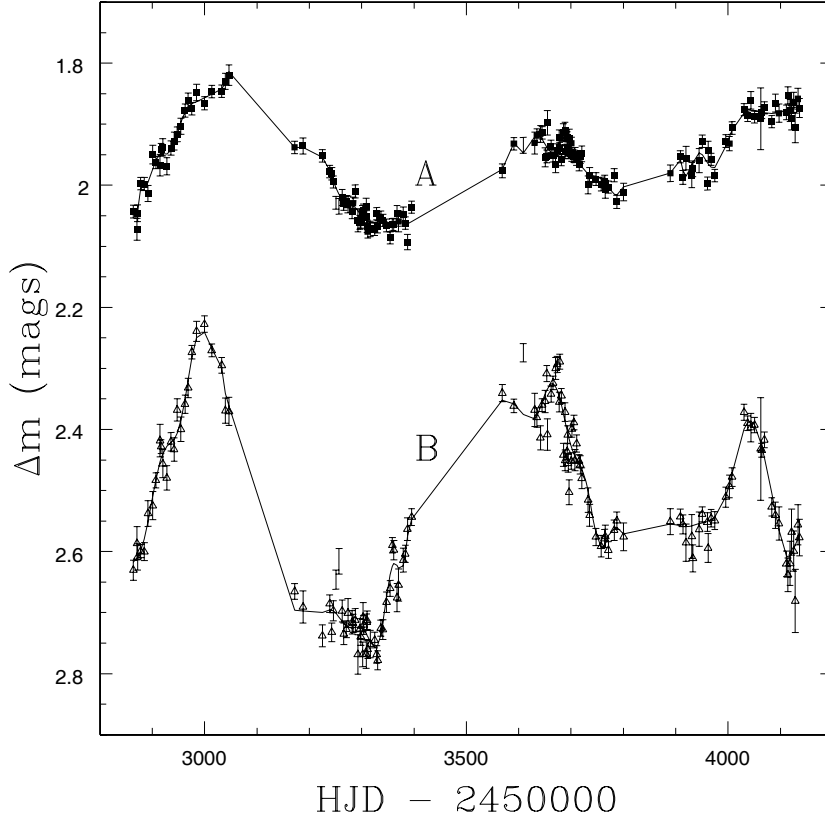


Fig. 6.— *R*-band lightcurves for QJ0158–4325 images A (squares) and B (triangles). The fits are drawn only to guide the eye. Data points with error bars only are cases of bright-sky contamination; they were not used in the microlensing analysis. “HJD” refers to the **Heliocentric Julian Date** reported in Tables 3 and 4.

or greater. On three nights, the data also suffered from contamination by bright sky conditions, resulting in low signal-to-noise for image B. These points were retained as part of the recorded data set but were omitted in the microlensing analysis.

To eliminate the limitations imposed by measuring absolute photometry, the image fluxes were measured relative to that of several reference stars in the same frame. In ground-based astronomy, the resolution is limited by atmospheric effects, so the quasar images and lens galaxy always overlap with each other (compare Figs. 4 and 5). It was therefore necessary to separate the quasar and galaxy images to measure the quasar image fluxes. This task was accomplished using the publicly available SExtractor and Image Reduction and Analysis Facility software packages and some self-authored processing scripts. The *HST* imagery was used to accurately determine the astrometry of the quasar images and reference stars in each frame. A point-spread function model consisting of three nested, elliptical Gaussian components was fit to the images and reference stars simultaneously. To eliminate the flux from the lens galaxy, a constant galaxy flux was

selected that minimized the aggregate residuals for each complete data set. The image fluxes were then measured from the best-fitting point-spread function models. Further details of the data reduction process are given in Kochanek et al. (2006). For QJ0158–4325, slight physical differences in the R -band filters used at each telescope gave rise to a “color term” that required a scaling of the values from the Euler telescope to match those from SMARTS. Once this scaling was accomplished, the two data sets were combined to obtain a plot of flux versus time for both quasar images. The new optical monitoring data for QJ0158–4325 and RXJ0911+0551 are presented in Appendix A in Tables 3 and 4, and the QJ0158–4325 lightcurves are displayed in Figure 6.

2.3. X-ray Observations

In addition to the optical monitoring data, several epochs of X-ray images for the systems RXJ0911+0551, B1422+0231, and HE0230–2130 were obtained from the publicly available *Chandra* data archive. The photometry of the X-ray images was measured by Pooley et al. (2007). The RXJ0911+0551 lightcurve includes two epochs of X-ray data taken about a year apart. The B1422+0231 lightcurve includes three epochs of X-ray data, and the HE0230–2130 lightcurve includes one. These data were used to complement the short optical lightcurves from the SMARTS and WIYN observatories.

3. Data Analysis

The five lenses were treated using variations of one technique. In §3.1, the generation of mass models to obtain microlensing parameters is discussed. The following section, §3.2, describes the Monte Carlo routine and Bayesian analysis used for all five systems. In §3.3, the lightcurve preparation and subsequent analysis used to estimate time delays in QJ0158–4325 and HE1104–1805 are described. Finally, §3.4 discusses the application of the method to simultaneously estimate X-ray and optical emission region sizes in HE0230–2130, B1422+0231, and RXJ0911+0551.

3.1. *HST* Images and Mass Models

For each object, a range of microlensing parameters in the lens galaxy were possible, so all needed to be tested. These parameters were yielded by macroscopic mass models generated using the *lensmodel* software package of Keeton (2001). The stellar component was represented by a de Vaucouleurs profile, and the dark matter was represented by a concentric NFW (Navarro, Frenk & White, 1996) dark matter profile. For each system, the ellipticity of the combined model was set to the axis ratio measured in the *HST* imagery, but it was permitted to change within the observed uncertainties to optimize the fit of

Lens	$f_{M/L}$	κ		γ		κ_*/κ	
		A	B	A	B	A	B
QJ0158–4325	0.1	0.73	0.99	0.19	0.29	0.030	0.074
	0.2	0.66	0.96	0.22	0.38	0.064	0.15
	0.3	0.63	0.94	0.23	0.44	0.086	0.20
	0.4	0.54	0.89	0.28	0.57	0.15	0.32
	0.5	0.48	0.86	0.30	0.67	0.21	0.42
	0.6	0.42	0.82	0.32	0.76	0.30	0.54
	0.7	0.35	0.78	0.35	0.85	0.41	0.65
	0.8	0.29	0.75	0.37	0.94	0.57	0.78
	0.9	0.23	0.72	0.39	1.03	0.81	0.92
	1.0	0.20	0.70	0.41	1.08	1.00	1.00
HE1104–1805	0.1	0.86	0.58	0.26	0.18	0.036	0.012
	0.2	0.80	0.53	0.33	0.18	0.079	0.027
	0.3	0.73	0.47	0.40	0.19	0.12	0.044
	0.4	0.67	0.41	0.47	0.19	0.18	0.064
	0.5	0.61	0.35	0.53	0.20	0.24	0.093
	0.6	0.55	0.30	0.60	0.20	0.32	0.13
	0.7	0.49	0.25	0.67	0.20	0.41	0.18
	0.8	0.43	0.19	0.73	0.21	0.53	0.26
	0.9	0.37	0.14	0.80	0.21	0.68	0.40
	1.0	0.30	0.07	0.88	0.21	1.00	1.00

Note. — Microlensing parameters for each of the QJ0158–4325 and HE1104–1805 macroscopic lens models. The variables are convergence (mean surface density) κ , shear γ and the fraction of the total surface density composed of stars κ_*/κ at the location of each image.

Table 2. Lens Galaxy Mass Models

the model. Since the dark matter fractions in the lens galaxies were unknown, a series of models were generated with a range of dark matter content from $0.1 \leq f_{\text{M/L}} \leq 1.0$, where $f_{\text{M/L}}$ represents the mass fraction in stars relative to that in a constant mass-to-light ratio model. Each model yielded the mean surface density (convergence) κ , gravitational shear γ , and surface density in stars κ_* (where $\kappa_* \leq \kappa$) at the locations of each image. As examples, the microlensing parameters generated for QJ0158–4325 and HE1104–1805 are presented in Table 2.

3.2. Microlensing Analysis Technique

The essence of the microlensing analysis was to generate large numbers of simulated microlensing light curves in an attempt to reproduce the observed microlensing variability. The simulated lightcurves were made using a range of plausible physical parameters and were then compared to the observed lightcurves. Bayesian methods were used to analyze the χ^2 statistics of the simulated lightcurves to obtain probability distributions for the quantities of interest – the time delays and emission region sizes. This approach is described briefly here, but a detailed description is available in Kochanek (2004).

3.2.1. Monte Carlo Routine

The parameters from the macroscopic mass models were used to create a set of microlensing magnification patterns in the source plane. First, random stellar distributions were generated based on the various parameter combinations. The stars were assumed to have an initial mass function $dN(M)/dM \propto M^{-1.3}$ over a mass range $M_1 < M < M_2$, with a dynamic range of $M_2/M_1 = 50$. This stellar mass function approximated the Galactic mass function of Gould (2000). The magnification patterns were then created using a variant of the ray-shooting method (Schneider et al., 1992) in which parallel light rays were computationally sent through the stellar distributions and collected on the source plane. A sample microlensing magnification pattern for QJ0158–4325 is shown in Figure 7. The superposition of the gravitational potentials of many stars led to complex patterns.

Next, large numbers of light curves were generated by moving source models through the magnification patterns over a range of velocities on random trajectories. The source model used for the optical emission was the face-on thin-disk surface brightness profile (Shakura & Sunyaev, 1973)

$$I(R) \propto \left\{ \exp \left[(R/r_s)^{3/4} \right] - 1 \right\}^{-1}, \quad (8)$$

which is based on the physical expectation that the optical emission comes from an accretion disk that radiates locally as a blackbody, as discussed in §1.1. Here, the scale length r_s is the radius at which the local disk blackbody temperature matches the **rest-frame effective wavelength** of the band being observed (given by $kT = hc(1 + z_s)/\lambda_{\text{obs}}$ for a source at

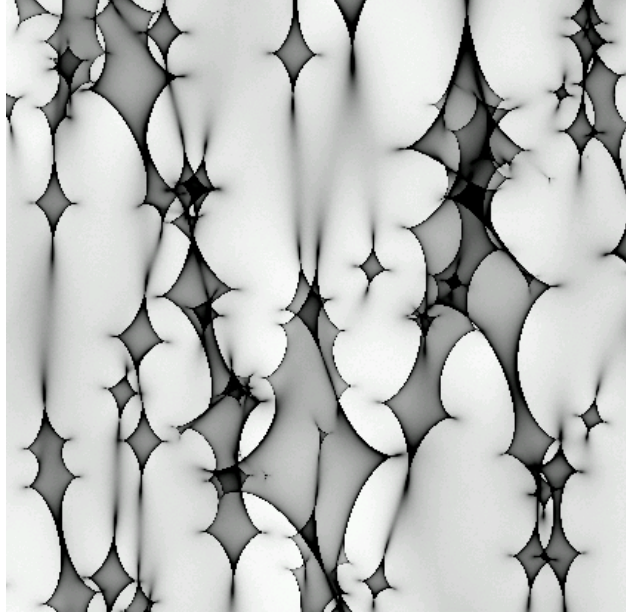


Fig. 7.— A region in a sample microlensing magnification pattern. This particular pattern was generated for a lens galaxy model with $f_{M/L}$ of 0.4.

redshift z_s). Microlensing is primarily sensitive to the projection of the source area onto the source plane, so the shape and inclination of the source must factor in to the calculation of r_s . For a thin disk inclined at an angle i relative to the line of sight, r_s scales as $\sqrt{\cos i}$. In this study, values of r_s are reported assuming the mean disk inclination angle of $\cos(i) = 1/2$. Five good fits to the lightcurves of QJ0158–4325 are shown in Figure 8.

The X-ray emission profile and shape are unknown; however, Mortonson et al. (2005) demonstrated that the **half-light radius** measured with microlensing is effectively independent of the surface brightness profile used in the model. For this analysis, then, the effective (i.e., ignoring shape and inclination corrections) half-light radius $r_{1/2,X}$ was chosen to characterize the X-ray emission. A thin-disk surface brightness profile was chosen as the emission model. In this model, the half-light radius is related to the scale radius by $r_{1/2,X} = 2.44r_s$.

Source models covering a range of sizes in both optical and X-ray wavelength bands were convolved with the raw point-source magnification patterns. Microlensing light curves were generated by running sources through the magnification patterns, using random starting points and effective velocities \mathbf{v}_e along the source plane. The effective velocities are the net result of the relative motions of the observer, lens galaxy, quasar, and lens galaxy stars projected onto the source plane. The Earth-bound observer’s velocity was determined from the **cosmic microwave background radiation** dipole (Kogut et al., 1993). The velocities of the lens and quasar host galaxies were estimated from a statistical model based on structure formation simulations $\sigma_p = 235/(1+z) \text{ km}^{-1} \text{ s}^{-1} \text{ Mpc}^{-1}$ (Kochanek, 2004). In determining the contribution of the lens galaxy stellar motions, the lens galaxy was

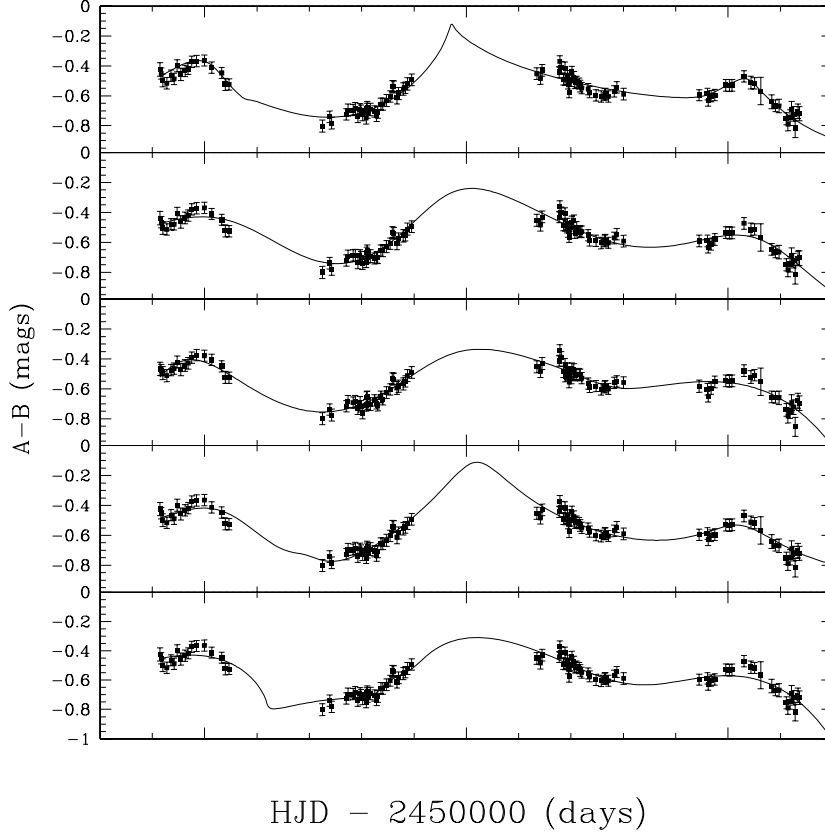


Fig. 8.— The five best trial microlensing light curve fits to the QJ0158–4325 microlensing signature obtained by taking the ratio of the A and B light curves shifted for a trial time delay of $\Delta t_{AB} = -20$ days.

assumed to be a dynamically relaxed system, so the velocity dispersion of the lens galaxy stars was set by the lens galaxy mass inferred from the lens model.

3.2.2. Parameter Estimation

Once the model curves were generated, the χ^2 statistic was computed for each of the trial light curves to yield a probability $P(D|\vec{p})$ of the data D given the model parameters \vec{p} for each trial curve. Next, Bayes's theorem and estimates of prior probabilities for the parameters, $P(\vec{p})$, were used to estimate probability distributions for the parameters given the data

$$P(\vec{p}|D) \propto \int P(D|\vec{p})P(\vec{p})d\vec{p}, \quad (9)$$

where $P(D|\vec{p})$ is the probability of fitting the data in a given trial and $P(\vec{p})$ represents the prior probabilities for the microlensing variables. The total probability was normalized such

that $\int P(\vec{p}|D)d\vec{p} = 1$. The Bayesian integrals were performed as a sum of the Monte Carlo trials over the microlensing parameters.

For all five lenses, the Bayesian analysis was performed to estimate a size for the optical emission region. In the cases of B1422+0231, HE0230–2130, and RXJ0911+0551, the objects were also analyzed for the size of their X-ray emission region. For each system, the analysis was performed both with and without application of a uniform prior on the mean mass of the microlensing stars $0.1M_{\odot} \leq \langle M \rangle \leq 1.0M_{\odot}$. In systems with long optical lightcurves showing significant variability, the size estimates with and without the prior were expected to be close. In systems with very little optical data, a large difference between the two was expected (see §4.4).

3.3. Time Delay Analysis of QJ0158–4325 and HE1104–1805

Prior to the Monte Carlo simulations, special preparation was required to estimate the time delays in QJ0158–4325 and HE1104–1805. The light curves for the multiple images exhibited the same intrinsic variability separated by a time delay, with the uncorrelated microlensing variability superimposed on the intrinsic variability. Therefore, shifting the two curves to compensate for the time delay and taking their ratio would leave only the differential microlensing signal. This was the basis for the first part of the approach to estimating the QJ0158–4325 and HE1104–1805 delays.

A technique was developed to shift the curves in each system by an arbitrary delay. This permitted the extraction of the microlensing signals implied by various possible delay values. The script to implement this shifting technique was written in *perl*. For each lens, the range of delays to be tested was drawn from the mass models based upon the astrometry and photometry of the *HST* images. HE1104–1805 was tested over a delay range of $125 \text{ days} \leq \Delta t_{AB} \leq 200 \text{ days}$, sampling at 1.5-day intervals. The lens models predicted a 2-3 week delay for QJ0158–4325, so delays of $-50 \leq \Delta t_{AB} \leq 50 \text{ days}$ were tested. For both lenses, $\Delta t_{AB} = t_A - t_B$, so positive delays imply that image A lags image B.

The first problem with this method is common to all types of time delay estimates. When the light curve for one of the images is shifted by an arbitrary delay value, the shifted data points are no longer temporally aligned with the unshifted points of the other image. Temporally aligned points were required in order to find the flux ratio between the two curves, so it was necessary to develop a reasonable interpolation scheme for one of the curves. Any kind of polynomial or spline fitting to find interpolated values would result in an artificial smoothing of the data for the interpolated curve, so linear interpolation was chosen for points falling within an observing season. Uncertainties were assigned to the interpolated flux values based upon the uncertainties of the bracketing points according to the relation

$$\sigma_m^2 = \frac{\sigma_i^2 (F_i - F_m)^2}{(F_i - F_{i+1})^2} + \frac{\sigma_{i+1}^2 (F_{i+1} - F_m)^2}{(F_i - F_{i+1})^2}, \quad (10)$$

where F_i , F_{i+1} , σ_i , and σ_{i+1} are the fluxes of the bracketing unshifted points and their associated uncertainties and F_m and σ_m are the shifted point and associated uncertainty.

The second problem was caused by gaps between observing seasons, when the quasar was obscured by the sun (i.e., when it transited the sky during daylight hours). Interpolating between seasons was not an option, since season gaps spanned several months. This left the choices of truncating the data or extrapolating based upon the unshifted data. Truncation was unattractive because it involved discarding data, while extrapolation required a substantial increase in error bar size with increasing temporal distance from the beginning or end of the season. A choice between these extremes was used. A linear extrapolation was performed based on the five data points nearest to the season gap, and extrapolations were limited to seven days. Existing photometric errors of the inter-season shifted points were combined with the uncertainties due to the temporal distance of the extrapolation from existing data points using the quasar structure function of Vanden Berk et al. (2004)

$$V(\Delta\tau) = \left(\frac{\Delta\tau}{\Delta\tau_0}\right)^\gamma, \quad (11)$$

which quantifies the expected quasar variability with time lag. For the purposes of the extrapolation, $\Delta\tau$ was the temporal distance of an extrapolated point into the season gap and $\Delta\tau_0$ and γ were determined by Vanden Berk et al. (2004) at 7×10^4 days and 0.336, respectively. The seven-day truncation limit prevented an excess of points with very large error bars, which would have significantly altered the statistical weights of extrapolated points and caused the fitting to favor longer delays.

For a standard analysis, the same number of data points were used for each delay. In all cases, the data used were restricted to the permissible epochs in the delay shift with the fewest usable points. It would seem that this “most limiting delay” would also be the longest delay, since longer delays push more points into the inter-season gap and past the extrapolation limit. This was not the case for HE1104–1805, where the delay range to be tested included large shifts that pushed data across the gap and into the neighboring season. For HE1104–1805, then, the data was restricted to that allowed by both the longest delay and the most limiting delay. In all, the interpolation and extrapolation scheme left 219 epochs for HE1104–1805 and 102 epochs for QJ0158–4325. Light curves with no limits on extrapolation were also tested.

The end result of this processing was a set of light curves shifted for a range of possible time delays. The set of microlensing light curves generated by this method was the data to which simulated microlensing light curves were compared. The probability of a given time delay is

$$P(\Delta t|D) \propto \int P(D|\vec{p}, \Delta t) P(\vec{p}) P(\Delta t) d\vec{p}, \quad (12)$$

where $P(\Delta t)$ is a uniform prior probability on the time delay from the mass models and $P(D|\vec{p}, \Delta t)$ is the probability of fitting the data in a particular trial.

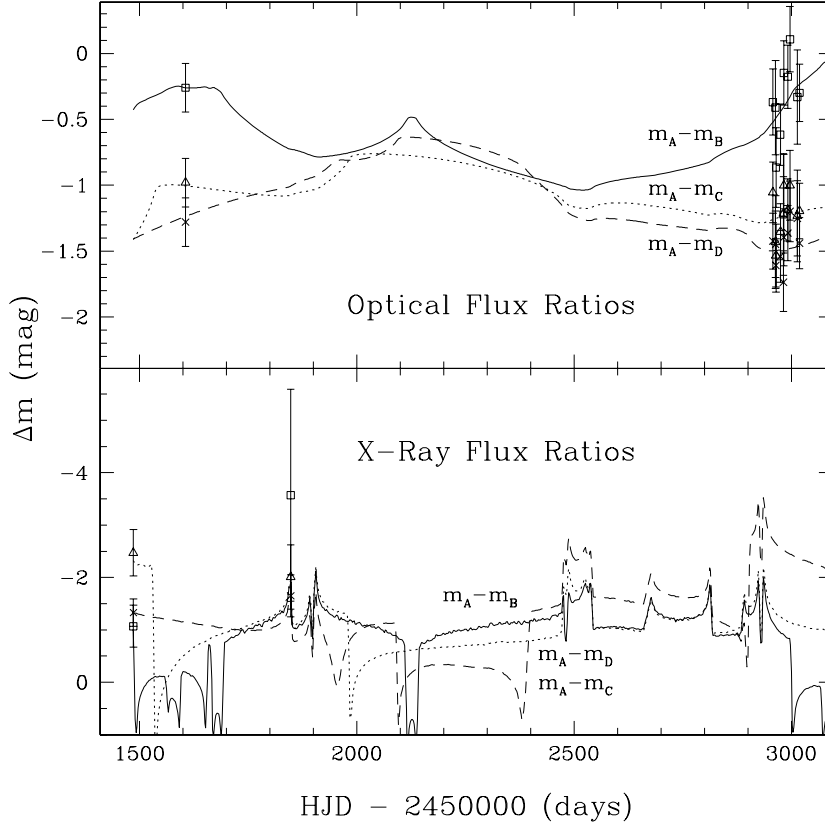


Fig. 9.— An example of a good fit to the microlensing light curves of RXJ0911+0551. The higher amplitude and shorter timescale of the X-ray microlensing relative to that in the optical is clearly visible in the curves generated by the simulations. The solid, dotted, and dashed curves represent the A-B, A-C, and A-D image flux ratios, respectively.

3.4. Joint X-Ray/Optical Analysis of HE0230–2130, B1422+0231, and RXJ0911+0551

As discussed in §2, the data for the lenses B1422+0231, HE0230–2130, and RXJ0911+0551 consisted of several epochs of optical and X-ray data. The X-ray-emitting regions of quasars are thought to be very small relative to typical stellar Einstein radii, so the microlensing variability in X-rays is expected to have a larger amplitude and shorter timescale than the variability at optical wavelengths. The strong X-ray variability overwhelms the slower, smaller-amplitude intrinsic variability, rendering the effects of the time delays statistically insignificant. Because of this fact and practical difficulties with shifting sparsely sampled light curves, no time delay corrections were made in these instances. An example of a good fit to the optical and X-ray curves of RXJ0911+0551 is shown in Figure 9.

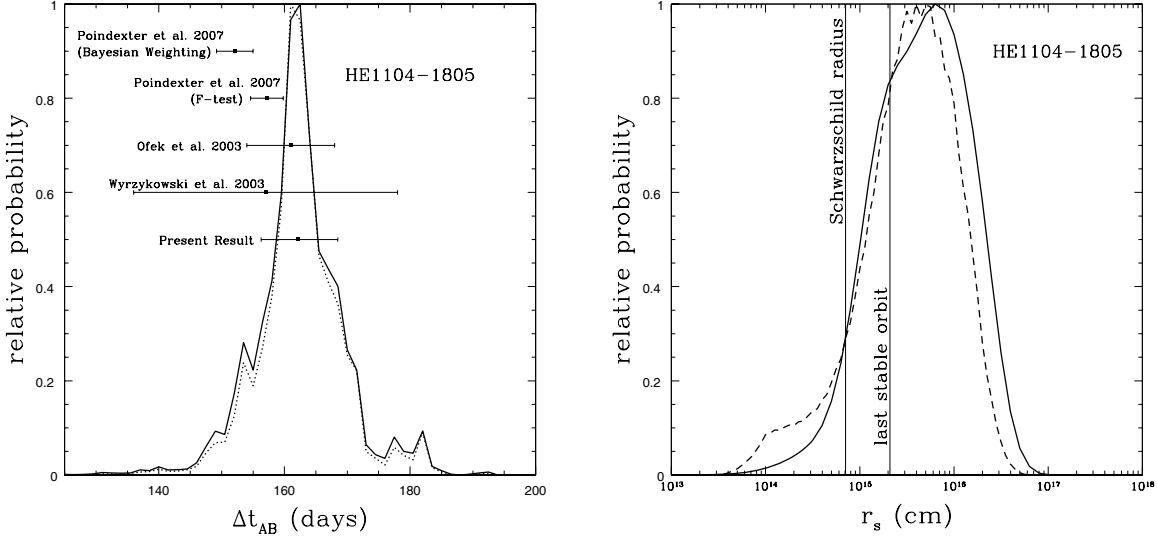


Fig. 10.— *Left panel:* Probability distribution for the time delay of HE1104–1805. The dotted curve assumes the uniform mass prior for the lens stars over the range $0.1M_\odot \leq \langle M \rangle \leq 1.0M_\odot$, while the solid curve assumes no prior. Both converge on the same value. Earlier results are plotted for comparison. The polynomial fitting estimates by Poindexter et al. (2007) depend on the statistical test used, while the Monte Carlo method employs a physical model to generate the microlensing signal. *Right panel:* Probability distribution for the HE1104–1805 source size at $0.2 \mu\text{m}$ both with (dashed curve) and without (solid curve) the microlens mass prior. They converge on consistent values. The Schwarzschild radius and innermost stable circular orbit are plotted for a black hole mass of $M_{\text{BH}} = 2.37 \times 10^9 M_\odot$ (Peng et al., 2006).

4. Results

4.1. HE1104–1805

The probability distribution for the time delay in HE1104–1805 is presented in Figure 10. To within 1σ , the time delay is $\Delta t_{AB} = t_A - t_B = 162.2^{+6.3}_{-5.9}$ days, in marginal agreement with the polynomial-fitting estimate of $\Delta t_{AB} = 152.2^{+2.8}_{-3.0}$ days of Poindexter et al. (2007) that used Bayesian weighting for the polynomial orders. The present estimate is in much better agreement with the Poindexter et al. (2007) result of 157.2 ± 2.6 days, which used the **F-test** to select among the different orders. It should be noted that the present approach uses a physical model for the microlensing rather than a polynomial parameterization, as in earlier estimates. The variance of the delay value in the Poindexter et al. (2007) study clearly indicates the dependence of their estimate on the parameterization used.

The present analysis also yielded a source size estimate of $\log[(r_s/\text{cm})\sqrt{\cos i/0.5}] = 15.7^{+0.4}_{-0.5}$ at a rest-frame wavelength of $0.2 \mu\text{m}$ (Fig. 10). This estimate is consistent with

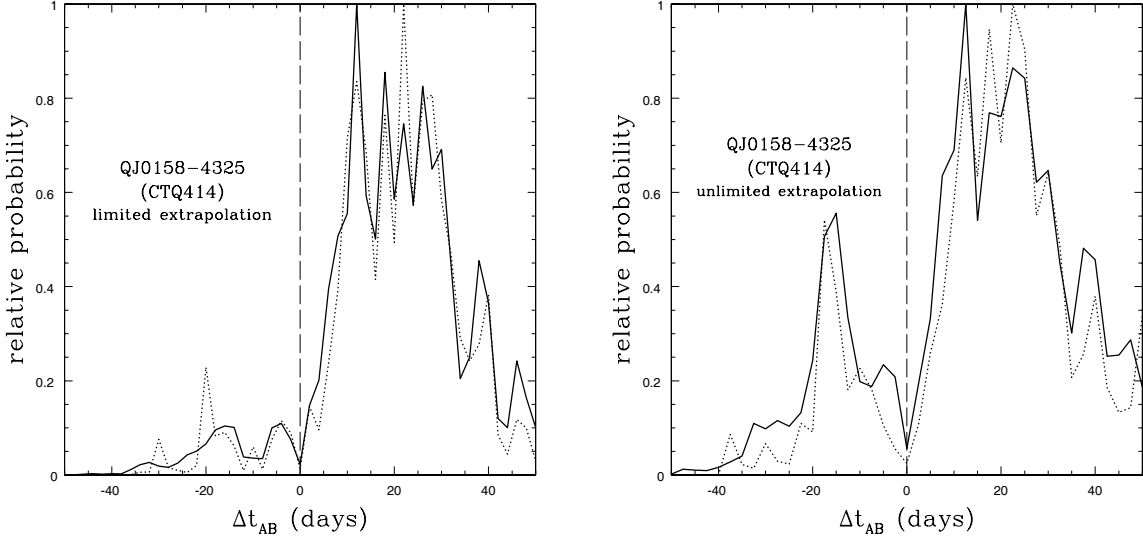


Fig. 11.— Probability distributions for the QJ0158–4325 time delay both with (dotted curves) and without (solid curves) the microlens mass prior, using limited and unlimited extrapolation. Both fail to converge on a single delay value and favor a positive sense for the delay, in direct contradiction to the predictions of the lens models.

earlier size estimates that used the Poindexter et al. (2007) delay value (Morgan et al., 2007; Poindexter, Morgan & Kochanek, 2007). The consistency of the disk size and the time delay estimates with earlier determinations validates the Monte Carlo technique.

4.2. QJ0158–4325

Probability distributions for time delay in QJ0158–4325 are displayed in Figure 11. The similar amplitude and timescale of the intrinsic and microlensing variability permitted the Monte Carlo simulation to find many reasonable lightcurve fits at a broad range of delays, so the fits did not converge on a most likely delay value. Positive delays $\Delta t_{AB} = t_A - t_B$ are favored over negative delays, a result which directly contradicts the prediction of the lens model. The results were generated using the limited extrapolation described earlier, as well as an unlimited extrapolation to test the effect of the truncation. The unlimited extrapolation tests yielded higher relative probabilities for negative delays, but the results still failed to converge on a single delay value. The project was therefore unsuccessful in estimating a time delay for QJ0158–4325. A time delay estimate will become possible when the source exhibits more high-amplitude intrinsic variability.

Whereas the strong microlensing prevented the estimation of a time delay, it enabled the estimation of an accretion disk size. Probability distributions for the disk size are shown in Figure 12. The large amplitude of the variability constrained the results to a small range

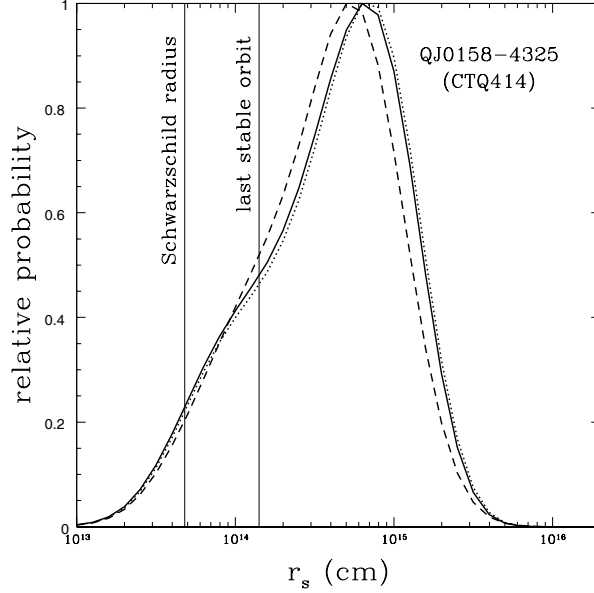


Fig. 12.— Probability distribution for the QJ0158–4325 source size at $0.3 \mu\text{m}$. The distributions for negative (dashed), positive (dotted), and combined sets of trial time delays converge on consistent values. As with HE1104–1805, the estimated emission region size lies outside the Schwarzschild radius and innermost stable circular orbit for this black hole, whose mass was estimated at $1.6 \times 10^8 M_\odot$ by Peng et al. (2006).

of source sizes, $\log[(r_s/\text{cm})\sqrt{\cos i/0.5}] = 14.9 \pm 0.3$ centered around $0.3 \mu\text{m}$. This result is physically sensible; it is consistent with expectations of Shakura & Sunyaev (1973), and it falls outside of the innermost stable circular orbit around the black hole. Additionally, the successful disk size estimates for both QJ0158–4325 and HE1104–1805 demonstrate the utility of this method in systems with undetermined time delays. The QJ0158–4325 and HE1104–1805 results were published in Morgan et al. (2008a).

4.3. X-ray Fitting Results

Probability distributions for the X-ray sizes in HE0230–2130 and B1422+0231 are displayed in Figure 13. Only one epoch of useful optical data was available for each of these systems, so the simulations failed to converge on optical disk sizes, but they did yield X-ray emission region sizes. Unfortunately, the X-ray results were sensitive to the application of the microlens mass prior. Results with the prior of $0.1 M_\odot \leq \langle M \rangle \leq 1.0 M_\odot$ are reported here. A size of $\log[R_{1/2,X}/\text{cm}] = 15.4 \pm 0.7$ was found for HE0230–2130, and a size of $\log[R_{1/2,X}/\text{cm}] = 15.7^{+0.6}_{-0.7}$ was found for B1422+0231. The large uncertainties are a direct result of the sparseness of the X-ray data.

Since eleven epochs of optical data were available in RXJ0911+0551, both

X-ray and optical sizes were successfully estimated. In the optical, a disk size of $\log[(r_s/\text{cm})\sqrt{\cos i/0.5}] = 16.1^{+0.4}_{-0.5}$ was yielded at $0.2\mu\text{m}$, while a size of $\log[R_{1/2,X}/\text{cm}] = 15.0^{+0.7}_{-0.8}$ was estimated at X-ray wavelengths. Again, the sparse X-ray data led to large uncertainties. A probability distribution for the ratio of the effective radii r_{opt}/r_X in RXJ0911+0551 is plotted in Figure 14. The size ratio was estimated to be $\log[r_{\text{opt}}/r_X] = 1.8^{+1.4}_{-0.9}$. This ratio is close to the ratio of $\log[r_{\text{opt}}/r_X] = 1.2^{+0.7}_{-0.4}$ found by Morgan et al. (2008b) in PG1115+080.

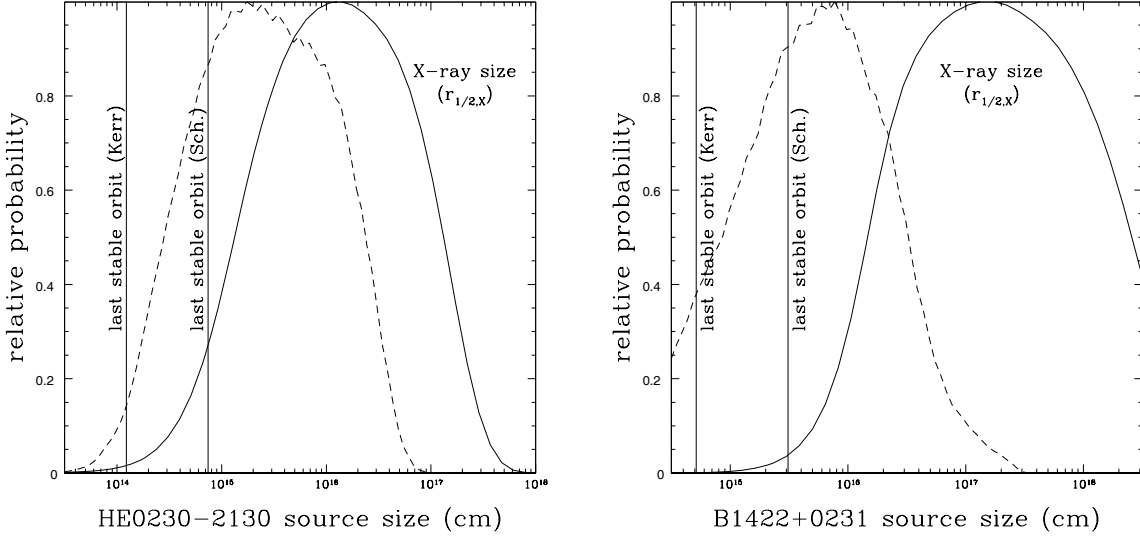


Fig. 13.— X-ray size probability distributions in HE0230-2130 and B1422+0231, both with (dashed) and without (solid) the microlens mass prior. The radii of the innermost stable circular orbits in both the Kerr and Schwarzschild metrics are included for comparison.

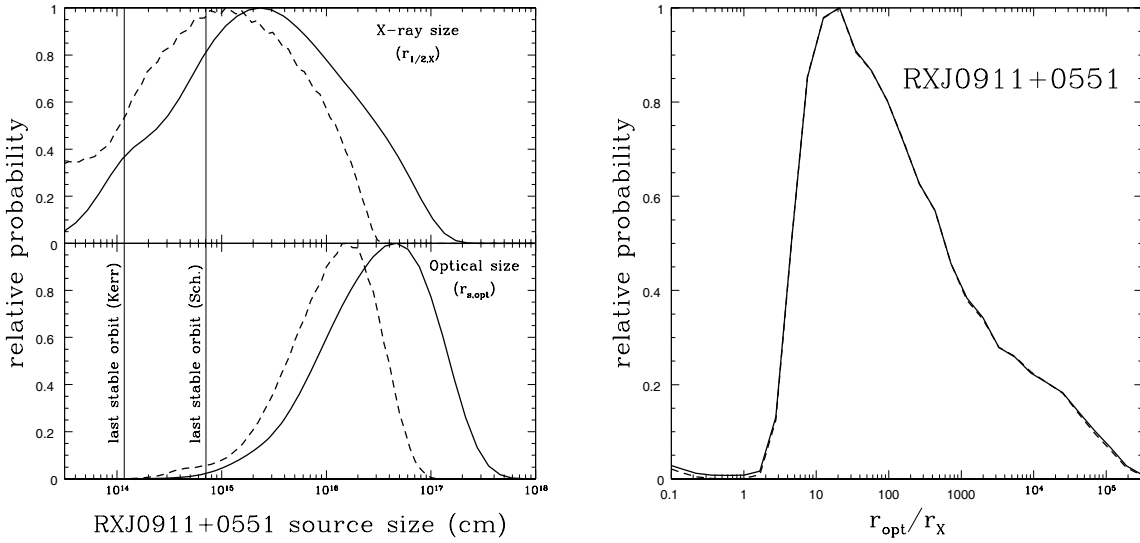


Fig. 14.— Probability distributions for the X-ray and optical sizes in RXJ0911+0551 and the ratio of the effective radii, again with (dashed) and without (solid) the microlens mass prior.

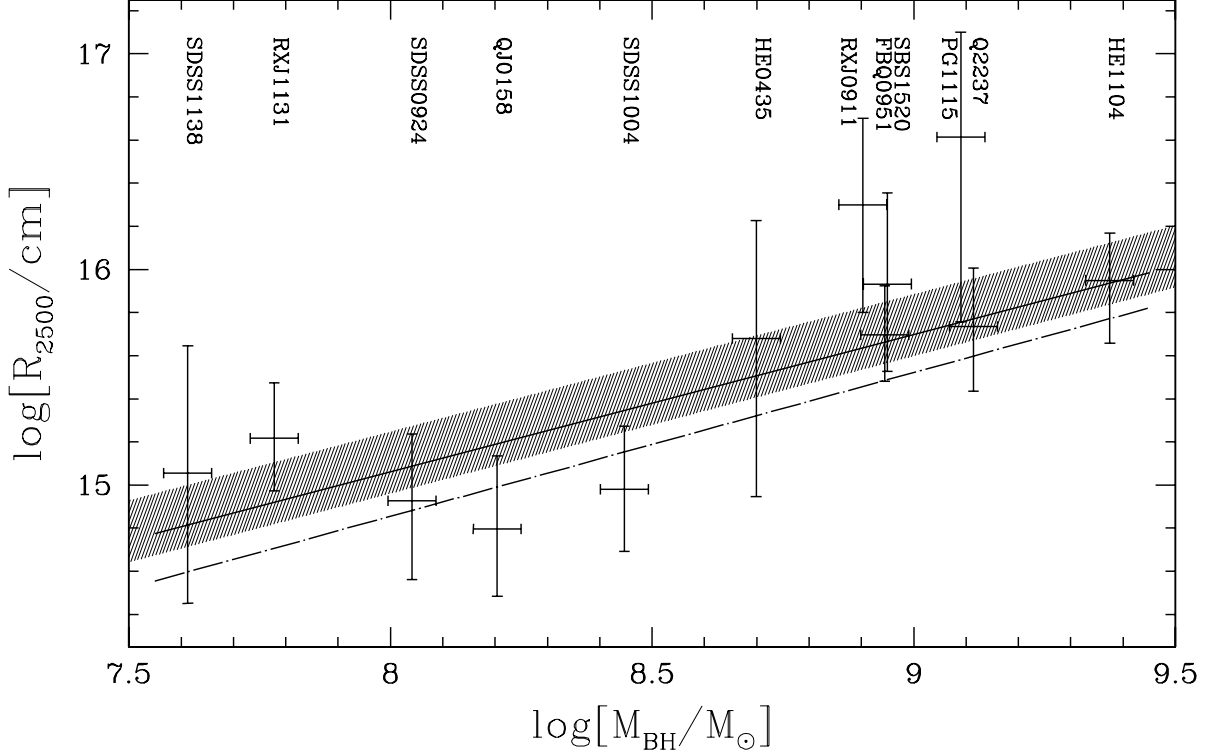


Fig. 15.— An updated plot based on the results of Morgan et al. (2007) showing the inclination-corrected accretion disk radii at $\lambda_{rest} = 2500 \text{ \AA}$ vs. black hole mass, reproduced here with the permission of C. Morgan. This plot includes the new QJ0158–4325 and RXJ0911+0551 points added by this study. The fit is a solid line, and the shaded region shows the variance due to disk inclination. The dot-dashed line represents the prediction of thin-disk theory for disks radiating at **Eddington luminosity** and an efficiency of 10%.

4.4. Discussion

The success of the Monte Carlo method in estimating both the time delay and disk size estimates in HE1104–1805 indicates that the method is a sound physical model for microlensing variability. Unlike the polynomial analyses used in other methods, the present results do not depend on the polynomial model used. Along with the larger error bars in the current result, this dependence indicates that the errors in the earlier estimates were likely underestimated, a concern that was noted by Poindexter, Morgan & Kochanek (2007).

The QJ0158–4325 and HE1104–1805 accretion disk size estimates are consistent with the predictions of the accretion disk size–black hole mass relation of Morgan et al. (2007). Based on emission line width-based quasar central black hole mass estimates

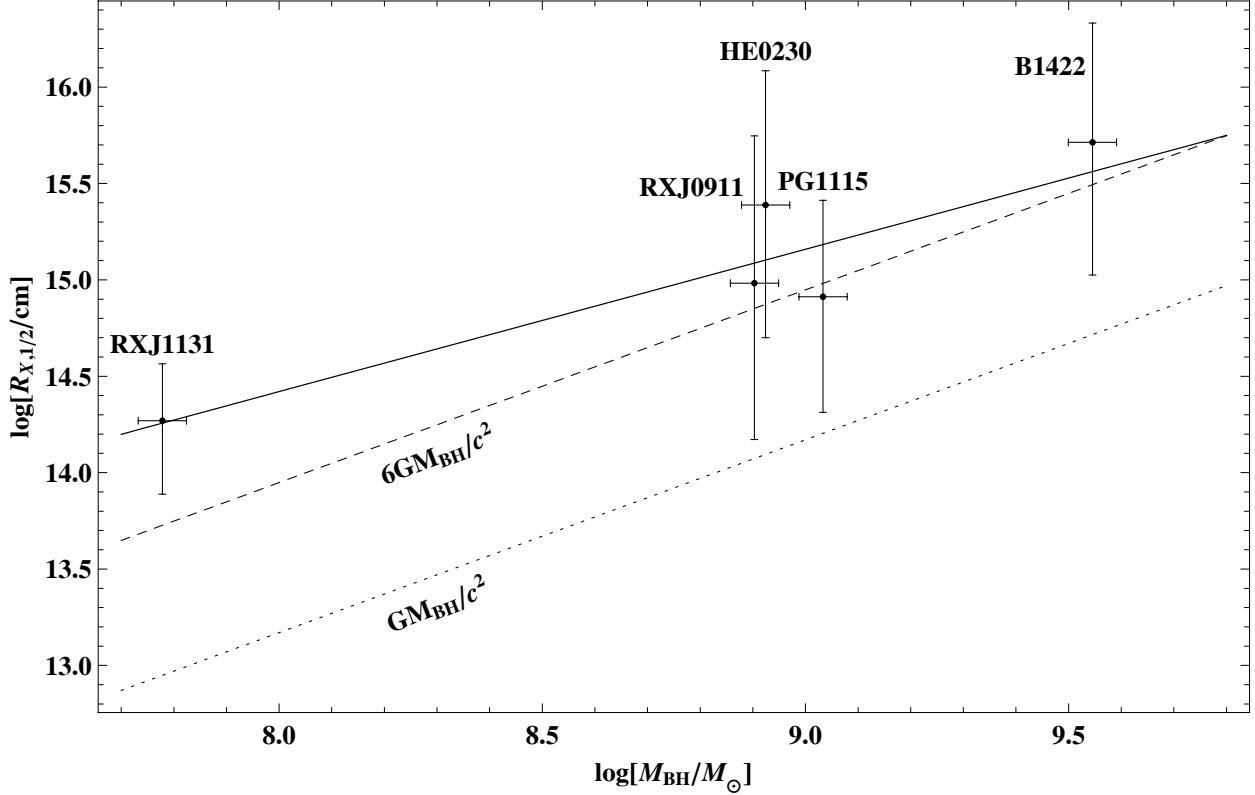


Fig. 16.— A plot of X-ray emission region size with black hole mass, including data from two quasars outside this study. The solid line is a power-law fit to the data. The dashed and dotted lines display the innermost stable circular orbit for a nonrotating black hole (Schwarzschild metric, $r_{\text{in}} = 6r_g = 6GM_{\text{BH}}/c^2$) and a maximally rotating black hole (Kerr metric, $r_{\text{in}} = r_g = GM_{\text{BH}}/c^2$), respectively.

of Peng et al. (2006), the correlation of Morgan et al. (2007) predicts source sizes of $\log[(r_s/\text{cm})\sqrt{\cos i/0.5}] = 15.9 \pm 0.2$ and 15.2 ± 0.2 at $2.5 \mu\text{m}$ for HE1104–1805 and QJ0158–4325, respectively. Scaling the r_s estimates of this project to this wavelength using the $R_{\lambda} \propto \lambda^{4/3}$ scaling from thin-disk theory yields disk sizes of $\log[(r_s/\text{cm})\sqrt{\cos i/0.5}] = 15.9^{+0.4}_{-0.5}$ for HE1104–1805 and $\log[(r_s/\text{cm})\sqrt{\cos i/0.5}] = 14.8 \pm 0.3$ for QJ0158–4325. The consistency of these estimates with the predictions confirm the validity of the Morgan et al. (2007) correlation and represent a significant step toward a full understanding of quasar accretion disks. These estimates are also significant because they demonstrate the possibility of making accretion disk size estimates in systems with unknown time delays.

In the cases of B1422+0231 and HE0230–2130, there is a large difference between the X-ray results obtained with and without a prior on the mean mass of the microlensing stars. This difference is attributed to the availability of only a single epoch of optical data in both cases, which allowed the simulations to easily fit the optical data with large source

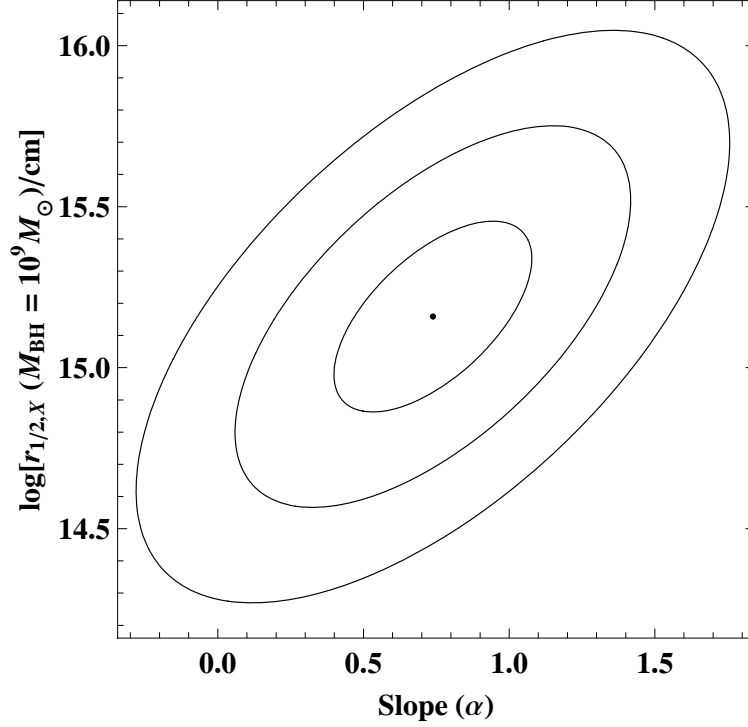


Fig. 17.— Confidence contours (1σ , 2σ , and 3σ) for the fits to the X-ray size as a function of black hole mass. The quantities $\log[r_{1/2,X}(M_{BH} = 10^9 M_{\odot})/\text{cm}]$ and α represent the intercept and slope, respectively, of the power-law fit to the data in Figure 16.

sizes, even at unreasonably high velocities. The large numbers of high-velocity solutions permitted fitting using large X-ray sources to match the observed X-ray flux ratios, pushing the X-ray distributions toward larger sizes. The application of the uniform microlens mass prior $0.1 M_{\odot} \leq \langle M \rangle \leq 1.0 M_{\odot}$ gave more weight to physically realistic velocities, resulting in much smaller size estimates. The failure of the simulations to converge on optical sizes for these two systems is attributed to a similar effect.

Scaling the RXJ0911+0551 optical estimate yields a $2.5\text{-}\mu\text{m}$ size of $\log[(r_s/\text{cm})\sqrt{\cos i/0.5}] = 16.3^{+0.4}_{-0.5}$, marginally inconsistent with the Morgan et al. (2007) prediction of $\log[(r_s/\text{cm})\sqrt{\cos i/0.5}] = 15.5 \pm 0.2$ based on a black hole mass of $M_{BH} = 8.0 \times 10^8 M_{\odot}$ from Peng et al. (2006). This inconsistency may be attributable to the sparseness of the optical data, but it is also easily explained by the variance introduced by the uncertain disk inclination angle. The new QJ0158–4325 and RXJ0911+0551 data points are plotted on the accretion disk size–black hole mass relation in Figure 15.

The possibility of an X-ray continuum size trend with mass was also tested. The new estimates from this study were combined with sizes for PG1115+080 and RXJ1131–1231, estimated by Morgan et al. (2008b) and Kochanek (in preparation, 2008), respectively. As displayed in Figure 16, the X-ray sizes show a strong correlation with black hole mass

$\log[r_{1/2,X}/cm] = (15.2 \pm 0.2) + (0.74 \pm 0.28) \log[M_{\text{BH}}/10^9 M_{\odot}]$. Confidence contours for the fit are plotted in Figure 17. The best fit lies close to the Schwarzschild innermost stable circular orbit at $6r_g$. This indicates that X-ray emission models with large emission regions are unlikely, such as the dragging-jet model of Hawley & Balbus (2002) or disk-corona models (e.g., Haardt & Maraschi, 1991; Merloni, 2003). The smaller “lamp-post” and “aborted jet” models of Martocchia et al. (2002) and Ghisellini et al. (2004) and the relativistic magnetohydrodynamic model of Hirose et al. (2004) are favored by the current results. Interestingly, the size-mass trend draws closer to the Schwarzschild innermost stable circular orbit with increasing black hole mass, however the slope of the correlation has a large uncertainty. Additional data will refine this uncertainty.

5. Conclusions

The successful optical and X-ray estimates confirm the usefulness of the Monte Carlo method as a tool for microlensing analysis in both optical-only and simultaneous X-ray/optical modes. The optical size estimates for QJ0158–4325 and HE1104–1805 are consistent with the trend of Morgan et al. (2007), confirming the relationship between accretion disk size and central black hole mass. Continued monitoring of QJ0158–4325 to capture higher-amplitude intrinsic variability may allow for a future estimate of the time delay in that system.

The X-ray results confirm that quasar X-ray emission regions are indeed much smaller than the optical regions, lying near the innermost stable circular orbit in the Schwarzschild metric. The X-ray sizes also follow a trend of increasing size with black hole mass, but at a shallower slope than the innermost stable circular orbit.

References

- Blaes, O. 2007 in *The Central Engine of Active Galactic Nuclei*, ed. L.C. Ho & J.-M. Wang (San Francisco: ASP), in press
- Blandford, R.D., Kochanek, C.S., Kovner, I., & Narayan, R. 1989, *Science*, 245, 824
- Bode, P., Bahcall, N.A., Ford, E.B., & Ostriker, J.P. 2001, *ApJ*, 551, 15
- Burud, I., Magain, P., Sohy, S. & Hjorth, J. 2001, *A&A*, 380, 805
- DePoy, D.L., Atwood, B., Belville, S.R., Brewer, D.F., Byard, P.L., Gould, A., Mason, J.A., O'Brien, T.P., Pappalardo, D.P., Pogge, R.W., Steinbrecher, D.P., & Tiega, E.J. 2003, *Proc. SPIE*, 4841, 827
- Eigenbrod, A., Courbin, F., Vuissoz, C., Meylan, G., Saha, P. & Dye, S. 2005, *A&A*, 436, 25
- Elvis, M. et al. 1994, *ApJS*, 95, 1
- Falco, E.E., Kochanek, C.S., Lehár, J., McLeod, B.A., Muñoz, J.A., Impey, C.D., Keeton, C., Peng C.Y., & Rix, H.-W. 2001, *The Castles Gravitational Lensing Tool*, from the ASP Conference Proceedings, Vol. 237, T.G. Brainerd & C.S. Kochanek, eds. (San Francisco:ASP)
- Ghisellini, G., Haardt, F. & Matt, G. 2004, *A&A*, 413, 535
- Gould, A. 2000, *ApJ*, 535, 928
- Haardt, F. & Maraschi, L. 1991, *ApJ*, 380, 51
- Hawley, J.F. & Balbus, S.A. 2002, 573, 738
- Hirose, S., Krolik, J.H., De Villiers, J.-P. & Hawley, J.F. 2004, *ApJ*, 606, 1083
- Keeton, C.R. 2001, preprint (astro-ph/0102340)
- Kochanek, C.S. 2004, *ApJ*, 605, 58
- Kochanek, C.S. & Schechter, P.L. 2004, *Measuring and Modeling the Universe*, from the Carnegie Observatories Centennial Symposia, W.L. Freedman, ed. (Cambridge UP: Cambridge) [astro-ph/0306040]
- Kochanek, C.S., Morgan, N.D., Falco, E.E. McLeod, B.A., Winn, J. Dembicky, J. & Ketzeback, B. 2006, *ApJ*, 640, 47
- Kochanek, C.S., Dai, X., Morgan, C.W., Morgan, N.D., Poindexter, S.A., Chartas, G. 2007, in *Statistical Challenges in Astronomy IV*, ed. G.J. Babu & E.D. Feigelson, (San Francisco:ASP), in press
- Kogut, A., et al. 1993, *ApJ*, 419, 1

- Lehár, J., Falco, E.E., Kochanek, C.S., McLeod, B.A., Impey, C.D., Rix, H.-W., Keeton, C.R. & Peng, C.Y. 2000, *ApJ*, 536, 584
- Martocchia, A., Matt, G. & Karas, V. 2002, *A&A*, 383, L23
- Merloni, A. 2003, *MNRAS*, 341, 1051
- Morgan, C.W., Kochanek, C.S., Morgan, N.D. & Falco, E.E. 2007, *ApJ*, submitted
- Morgan, C.W., Eyler, M.E., Kochanek, C.S., Morgan, N.D., Falco, E.E., Vuissoz, C., Courbin, F., & Meylan, G. 2008a, *ApJ*, 676, 80
- Morgan, C.W., Kochanek, C.S., Dai, X., Morgan, N.D. & Falco, E.E. 2008b, *ApJ*, submitted
- Mortonson, M.J., Schechter, P.L. & Wambsganss, J. 2005, *ApJ*, 628, 594
- Navarro, J.F. Frenk, C.S. & White S.D.M. 1996, *ApJ*, 462, 563
- Paraficz D., Hjorth J., Burud I., Jakobsson P., Elíasdóttir Á. 2006, *A&A*, 455, L1
- Peebles, P.J.E. 1993, *Principles of Physical Cosmology* (Princeton UP: Princeton)
- Peng, C.Y., Impey, C.D., Rix, H.-W., Kochanek, C.S., Keeton, C.S., Falco, E.E., Lehár, J. & McLeod, B.A. 2006, *ApJ*, 649, 616
- Peterson, B. M. 1997, *An Introduction to Active Galactic Nuclei* (Cambridge UP: Cambridge)
- Poindexter, S., Morgan, N.D. & Kochanek, C.S. 2007, *ApJ*, in press
- Poindexter, S., Morgan, N.D., Kochanek, C.S. & Falco, E.E 2007, *ApJ*, 660, 146
- Pooley, D., Blackburne, J. A., Rappaport, S. & Schechter, P.L. 2007 *ApJ*, 661, 19
- Refsdal, S. 1964, *MNRAS*, 128,307
- Shakura, N.I. & Sunyaev, R.A. 1973, *A&A*, 24, 337
- Schneider, P., Ehlers, J. & Falco, E.E. 1992, *Gravitational Lenses* (Berlin:Springer)
- Vanden Berk, D.E. et al. 2004, *ApJ*, 601, 692
- Wambsganss, J. 2005, in *Gravitational Lensing Impact on Cosmology*, from IAU Symposium, vol. 225, Mellier, Y. & Meylan, G., eds. (Cambridge UP: Cambridge)
- Wambsganss, J. 2006, in *Saas-Fee Advanced Course 33, Gravitational Lensing: Strong, Weak and Micro*, ed. G. Meylan, P. Jetzer. & P. North, (Berlin:Springer)
- Wyithe J. S. B., Turner E. L. 2001, *MNRAS*, 320, 21

APPENDIX A: MONITORING DATA

HJD	χ^2/N_{dof}	QSO A (mags)	QSO B (mags)	$\langle \text{Stars} \rangle$	Source
2863.873	1.17	2.043 ± 0.010	2.631 ± 0.015	-0.044 ± 0.003	SMARTS
2870.788	1.93	2.072 ± 0.013	2.585 ± 0.020	-0.050 ± 0.003	SMARTS
2871.813	0.66	2.046 ± 0.014	2.609 ± 0.022	-0.052 ± 0.003	SMARTS
2877.772	1.01	1.997 ± 0.008	2.600 ± 0.011	0.043 ± 0.002	SMARTS
2884.771	2.15	1.998 ± 0.007	2.600 ± 0.010	0.053 ± 0.002	SMARTS
2891.770	0.83	2.014 ± 0.013	2.537 ± 0.021	-0.055 ± 0.003	SMARTS
2900.798	2.26	1.950 ± 0.010	2.524 ± 0.015	-0.024 ± 0.003	SMARTS
2906.761	1.75	1.962 ± 0.007	2.483 ± 0.009	0.052 ± 0.002	SMARTS
2914.653	0.49	1.968 ± 0.018	2.417 ± 0.026	-0.038 ± 0.004	SMARTS
2916.766	1.00	1.942 ± 0.008	2.429 ± 0.011	0.018 ± 0.003	SMARTS
2919.787	0.55	1.938 ± 0.014	2.455 ± 0.023	-0.064 ± 0.003	SMARTS
2927.729	2.38	1.969 ± 0.009	2.479 ± 0.013	-0.005 ± 0.003	SMARTS
2935.680	2.25	1.939 ± 0.008	2.420 ± 0.010	0.034 ± 0.003	SMARTS
2941.674	3.82	1.928 ± 0.008	2.433 ± 0.010	0.046 ± 0.003	SMARTS
2947.635	0.73	1.916 ± 0.012	2.368 ± 0.018	-0.038 ± 0.003	SMARTS
2954.626	0.85	1.903 ± 0.013	2.400 ± 0.020	-0.050 ± 0.003	SMARTS
2962.598	1.28	1.878 ± 0.010	2.359 ± 0.013	-0.018 ± 0.003	SMARTS
2968.621	3.01	1.862 ± 0.007	2.332 ± 0.009	0.015 ± 0.003	SMARTS
2975.577	2.02	1.875 ± 0.007	2.273 ± 0.008	0.036 ± 0.003	SMARTS
2984.541	3.28	1.848 ± 0.007	2.239 ± 0.009	0.041 ± 0.003	SMARTS
2999.619	1.54	1.866 ± 0.009	2.227 ± 0.011	0.032 ± 0.003	SMARTS
3013.587	0.92	1.846 ± 0.008	2.271 ± 0.011	-0.012 ± 0.003	SMARTS
3032.567	1.70	1.846 ± 0.008	2.295 ± 0.010	0.033 ± 0.003	SMARTS
3039.534	1.34	1.830 ± 0.011	2.369 ± 0.018	-0.051 ± 0.003	SMARTS
3046.543	4.29	1.820 ± 0.008	2.371 ± 0.011	0.030 ± 0.003	SMARTS
3171.930	0.92	1.938 ± 0.008	2.666 ± 0.013	0.020 ± 0.003	SMARTS
3187.869	0.65	1.934 ± 0.013	2.694 ± 0.026	-0.050 ± 0.003	SMARTS
3224.869	0.70	1.950 ± 0.010	2.743 ± 0.018	-0.001 ± 0.003	SMARTS
3238.825	0.99	1.977 ± 0.009	2.688 ± 0.014	0.031 ± 0.003	SMARTS
3242.777	0.76	1.981 ± 0.009	2.732 ± 0.015	0.004 ± 0.003	SMARTS
3245.784	0.61	1.994 ± 0.010	2.698 ± 0.016	-0.036 ± 0.003	SMARTS
3250.779	1.29	(2.029 ± 0.009)	(2.646 ± 0.014)	-0.025 ± 0.003	SMARTS
3256.852	0.80	(2.035 ± 0.013)	(2.616 ± 0.021)	-0.025 ± 0.003	SMARTS

(cont'd)

Table 3. QJ0158–4325 R-band Lightcurves

Table 3—Continued

HJD	χ^2/N_{dof}	QSO A (mags)	QSO B (mags)	$\langle \text{Stars} \rangle$	Source
3262.779	3.42	2.020 ± 0.007	2.697 ± 0.010	0.048 ± 0.002	SMARTS
3265.790	1.82	2.030 ± 0.008	2.735 ± 0.013	0.021 ± 0.003	SMARTS
3270.792	1.46	2.027 ± 0.008	2.727 ± 0.011	0.038 ± 0.003	SMARTS
3273.731	1.68	2.031 ± 0.011	2.701 ± 0.018	-0.029 ± 0.003	SMARTS
3281.769	1.52	2.043 ± 0.010	2.716 ± 0.016	-0.017 ± 0.003	SMARTS
3283.759	1.65	2.029 ± 0.008	2.718 ± 0.011	0.026 ± 0.003	SMARTS
3287.633	0.73	2.009 ± 0.011	2.715 ± 0.019	0.004 ± 0.003	SMARTS
3292.735	2.96	2.057 ± 0.011	2.769 ± 0.019	-0.017 ± 0.003	SMARTS
3296.721	2.25	2.061 ± 0.008	2.726 ± 0.011	0.037 ± 0.003	SMARTS
3298.691	1.36	2.060 ± 0.008	2.740 ± 0.012	0.028 ± 0.003	SMARTS
3301.686	0.84	2.044 ± 0.011	2.769 ± 0.020	-0.039 ± 0.003	SMARTS
3302.791	0.98	2.045 ± 0.013	2.700 ± 0.024	-0.104 ± 0.003	EULER
3303.690	0.80	2.041 ± 0.010	2.720 ± 0.016	-0.036 ± 0.003	SMARTS
3308.686	2.29	2.028 ± 0.009	2.761 ± 0.015	-0.101 ± 0.003	EULER
3309.642	0.58	2.051 ± 0.009	2.717 ± 0.013	-0.007 ± 0.003	SMARTS
3310.580	1.51	2.060 ± 0.008	2.706 ± 0.012	-0.048 ± 0.002	EULER
3311.639	1.88	2.076 ± 0.008	2.760 ± 0.011	0.041 ± 0.003	SMARTS
3316.694	0.59	2.071 ± 0.013	2.752 ± 0.022	-0.034 ± 0.003	SMARTS
3324.630	1.37	2.072 ± 0.008	2.745 ± 0.011	0.028 ± 0.003	SMARTS
3328.616	0.66	2.046 ± 0.009	2.769 ± 0.015	-0.002 ± 0.003	SMARTS
3330.629	1.05	2.068 ± 0.009	2.779 ± 0.015	-0.013 ± 0.003	SMARTS
3336.600	0.88	2.052 ± 0.009	2.726 ± 0.013	-0.015 ± 0.003	SMARTS
3340.603	0.96	2.058 ± 0.010	2.728 ± 0.016	0.017 ± 0.003	SMARTS
3347.574	0.83	2.065 ± 0.010	2.685 ± 0.017	0.007 ± 0.003	SMARTS
3354.564	1.45	2.086 ± 0.008	2.661 ± 0.011	0.031 ± 0.003	SMARTS
3358.560	1.00	2.064 ± 0.009	2.592 ± 0.012	0.004 ± 0.003	SMARTS
3361.553	0.73	2.063 ± 0.011	2.600 ± 0.016	-0.023 ± 0.003	SMARTS
3367.572	0.62	2.046 ± 0.014	2.677 ± 0.023	-0.048 ± 0.003	SMARTS
3370.582	2.26	2.057 ± 0.011	2.658 ± 0.018	-0.012 ± 0.003	SMARTS
3379.581	0.55	2.046 ± 0.012	2.619 ± 0.020	0.004 ± 0.003	SMARTS
3383.581	1.32	2.062 ± 0.009	2.604 ± 0.012	0.021 ± 0.003	SMARTS
3387.563	0.63	2.092 ± 0.012	2.566 ± 0.018	-0.025 ± 0.003	SMARTS
3395.547	0.86	2.036 ± 0.010	2.544 ± 0.014	-0.045 ± 0.003	SMARTS
3568.889	1.66	1.976 ± 0.009	2.340 ± 0.011	0.000 ± 0.003	SMARTS

(cont'd)

Table 3—Continued

HJD	χ^2/N_{dof}	QSO A (mags)	QSO B (mags)	$\langle \text{Stars} \rangle$	Source
3590.890	1.19	1.932 ± 0.008	2.362 ± 0.010	0.020 ± 0.003	SMARTS
3608.820	4.55	(1.928 ± 0.006)	(2.267 ± 0.007)	0.050 ± 0.002	EULER
3630.626	0.75	1.929 ± 0.018	2.370 ± 0.027	-0.041 ± 0.003	SMARTS
3634.802	0.86	1.918 ± 0.011	2.382 ± 0.016	-0.047 ± 0.003	SMARTS
3641.753	2.01	1.916 ± 0.010	2.414 ± 0.014	0.007 ± 0.003	SMARTS
3644.792	0.91	1.914 ± 0.008	2.360 ± 0.010	0.015 ± 0.003	SMARTS
3653.595	1.43	1.953 ± 0.009	2.309 ± 0.011	-0.007 ± 0.003	SMARTS
3661.717	0.77	1.936 ± 0.010	2.342 ± 0.013	-0.052 ± 0.003	SMARTS
3665.707	0.91	1.952 ± 0.009	2.324 ± 0.011	-0.023 ± 0.003	SMARTS
3670.620	1.53	1.964 ± 0.011	2.302 ± 0.015	-0.005 ± 0.003	SMARTS
3673.595	0.81	1.942 ± 0.011	2.294 ± 0.013	-0.020 ± 0.003	SMARTS
3677.661	3.41	1.915 ± 0.007	2.348 ± 0.009	0.080 ± 0.002	EULER
3678.644	1.28	1.939 ± 0.009	2.290 ± 0.011	0.017 ± 0.003	SMARTS
3681.643	0.88	1.958 ± 0.009	2.345 ± 0.012	-0.011 ± 0.003	SMARTS
3685.668	5.14	1.907 ± 0.006	2.435 ± 0.008	0.011 ± 0.002	EULER
3688.633	0.50	1.944 ± 0.011	2.373 ± 0.015	-0.050 ± 0.003	SMARTS
3688.676	4.26	1.903 ± 0.006	2.444 ± 0.008	0.000 ± 0.002	EULER
3692.631	2.72	1.916 ± 0.006	2.429 ± 0.008	0.032 ± 0.002	EULER
3693.560	2.10	1.941 ± 0.008	2.409 ± 0.010	0.012 ± 0.003	SMARTS
3694.631	2.43	1.939 ± 0.007	2.448 ± 0.009	0.058 ± 0.002	EULER
3696.623	5.99	1.916 ± 0.006	2.496 ± 0.008	0.087 ± 0.002	EULER
3700.648	2.38	1.924 ± 0.006	2.445 ± 0.009	0.068 ± 0.002	EULER
3701.605	1.01	1.951 ± 0.010	2.400 ± 0.013	-0.001 ± 0.003	SMARTS
3705.652	1.12	1.952 ± 0.009	2.389 ± 0.011	0.019 ± 0.003	SMARTS
3707.707	2.82	1.944 ± 0.007	2.443 ± 0.010	0.066 ± 0.002	EULER
3710.605	0.99	1.957 ± 0.010	2.424 ± 0.014	0.008 ± 0.003	SMARTS
3715.694	2.21	1.960 ± 0.006	2.445 ± 0.007	0.047 ± 0.002	EULER
3717.573	0.68	1.953 ± 0.010	2.459 ± 0.015	-0.048 ± 0.003	SMARTS
3720.644	3.80	1.942 ± 0.007	2.473 ± 0.009	-0.006 ± 0.002	EULER
3732.631	4.36	1.992 ± 0.007	2.509 ± 0.010	0.067 ± 0.002	EULER
3735.616	4.39	1.978 ± 0.006	2.534 ± 0.009	0.074 ± 0.002	EULER
3747.614	3.03	1.983 ± 0.006	2.569 ± 0.008	0.014 ± 0.002	EULER
3757.606	1.92	1.991 ± 0.008	2.584 ± 0.013	0.023 ± 0.002	EULER
3764.534	0.80	1.994 ± 0.010	2.579 ± 0.015	-0.015 ± 0.003	SMARTS

(cont'd)

Table 3—Continued

HJD	χ^2/N_{dof}	QSO A (mags)	QSO B (mags)	$\langle \text{Stars} \rangle$	Source
3765.570	6.22	2.000 ± 0.006	2.568 ± 0.007	0.080 ± 0.002	EULER
3771.604	2.31	1.996 ± 0.006	2.591 ± 0.009	0.031 ± 0.002	EULER
3782.557	1.59	1.977 ± 0.008	2.558 ± 0.013	-0.043 ± 0.002	EULER
3787.531	2.82	2.020 ± 0.006	2.542 ± 0.009	0.035 ± 0.002	EULER
3800.519	2.23	2.004 ± 0.010	2.569 ± 0.015	-0.044 ± 0.002	EULER
3889.922	2.68	1.973 ± 0.008	2.544 ± 0.013	0.036 ± 0.002	EULER
3908.910	2.44	1.946 ± 0.006	2.536 ± 0.008	0.070 ± 0.002	EULER
3913.839	2.94	1.980 ± 0.007	2.548 ± 0.009	0.042 ± 0.002	EULER
3919.880	5.01	1.949 ± 0.009	2.578 ± 0.014	-0.052 ± 0.002	EULER
3930.856	0.49	1.983 ± 0.021	2.577 ± 0.036	-0.001 ± 0.004	SMARTS
3932.920	1.40	1.966 ± 0.011	2.604 ± 0.019	-0.072 ± 0.002	EULER
3950.832	2.46	1.921 ± 0.006	2.532 ± 0.008	0.085 ± 0.002	EULER
3960.817	1.23	1.997 ± 0.010	2.552 ± 0.014	-0.034 ± 0.003	SMARTS
3961.922	6.26	1.937 ± 0.006	2.587 ± 0.009	0.030 ± 0.002	EULER
3967.838	0.85	1.957 ± 0.010	2.546 ± 0.014	-0.003 ± 0.003	SMARTS
3974.783	1.11	1.984 ± 0.010	2.550 ± 0.014	-0.009 ± 0.003	SMARTS
3995.765	0.88	1.927 ± 0.011	2.511 ± 0.016	-0.019 ± 0.003	SMARTS
4002.702	1.03	1.931 ± 0.012	2.494 ± 0.018	-0.023 ± 0.003	SMARTS
4007.696	0.70	1.905 ± 0.010	2.479 ± 0.015	-0.013 ± 0.003	SMARTS
4030.632	0.82	1.876 ± 0.010	2.372 ± 0.013	-0.003 ± 0.003	SMARTS
4037.600	0.92	1.886 ± 0.009	2.390 ± 0.012	-0.008 ± 0.003	SMARTS
4043.600	0.48	1.861 ± 0.015	2.397 ± 0.023	-0.056 ± 0.003	SMARTS
4050.620	1.34	1.888 ± 0.008	2.393 ± 0.011	0.002 ± 0.003	SMARTS
4062.536	0.47	1.891 ± 0.051	2.432 ± 0.084	0.151 ± 0.004	SMARTS
4064.646	0.84	1.881 ± 0.009	2.434 ± 0.012	0.006 ± 0.003	SMARTS
4069.580	0.82	1.872 ± 0.009	2.419 ± 0.013	-0.036 ± 0.003	SMARTS
4083.542	0.69	1.895 ± 0.010	2.527 ± 0.015	-0.019 ± 0.003	SMARTS
4090.621	2.29	1.865 ± 0.010	2.541 ± 0.014	-0.025 ± 0.003	SMARTS
4097.556	0.40	1.882 ± 0.015	2.554 ± 0.027	-0.045 ± 0.003	SMARTS
4111.601	1.23	1.880 ± 0.011	2.622 ± 0.019	-0.016 ± 0.003	SMARTS
4114.561	1.08	1.842 ± 0.013	2.664 ± 0.027	-0.024 ± 0.003	SMARTS
4118.593	0.48	1.873 ± 0.018	2.628 ± 0.036	-0.044 ± 0.003	SMARTS
4121.529	0.57	1.888 ± 0.020	2.571 ± 0.038	-0.044 ± 0.003	SMARTS
4125.526	0.66	1.863 ± 0.017	2.602 ± 0.033	-0.043 ± 0.003	SMARTS

(cont'd)

Table 3—Continued

HJD	χ^2/N_{dof}	QSO A (mags)	QSO B (mags)	$\langle \text{Stars} \rangle$	Source
4128.574	0.51	1.900 ± 0.024	2.696 ± 0.052	-0.039 ± 0.003	SMARTS
4133.581	0.45	1.858 ± 0.017	2.557 ± 0.033	-0.046 ± 0.003	SMARTS
4136.572	0.49	1.873 ± 0.015	2.578 ± 0.030	-0.061 ± 0.003	SMARTS
4301.869	1.05	1.815 ± 0.008	2.565 ± 0.012	0.021 ± 0.003	SMARTS
4307.824	0.70	1.794 ± 0.009	2.571 ± 0.016	-0.026 ± 0.003	SMARTS

Note. — “HJD” is the Heliocentric Julian Date – 2450000 days. The goodness of fit of the image per degree of freedom, χ^2/N_{dof} , is used to rescale the formal uncertainties when greater than unity. The QSO columns give the magnitudes of the quasar images relative to the reference stars. The $\langle \text{Stars} \rangle$ column gives the mean magnitude of the standard stars for that epoch relative to their mean for all epochs. A few points in the lightcurves (in parentheses) were not used in the analysis (see §2.2).

HJD	χ^2/N_{dof}	QSO A (mags)	QSO B (mags)	QSO C (mags)	QSO D (mags)	$\langle \text{Stars} \rangle$	Source
2957.750	3.03	3.394 ± 0.064	3.763 ± 0.085	4.448 ± 0.063	4.818 ± 0.036	0.002 ± 0.003	SMARTS
2963.750	3.40	3.313 ± 0.096	3.724 ± 0.141	4.744 ± 0.137	4.760 ± 0.031	0.002 ± 0.003	SMARTS
2964.750	3.08	3.167 ± 0.058	4.032 ± 0.130	4.701 ± 0.077	4.775 ± 0.025	0.003 ± 0.003	SMARTS
2969.750	0.74	2.971 ± 0.132	5.466 ± 1.547	4.026 ± 0.221	4.803 ± 0.155	-0.026 ± 0.003	SMARTS
2974.750	11.97	3.181 ± 0.023	3.797 ± 0.040	4.534 ± 0.029	4.721 ± 0.017	0.006 ± 0.003	SMARTS
2981.750	1.12	3.105 ± 0.118	4.327 ± 0.388	4.321 ± 0.177	4.841 ± 0.065	-0.004 ± 0.003	SMARTS
2982.750	2.49	3.421 ± 0.076	3.569 ± 0.081	4.423 ± 0.073	4.816 ± 0.040	0.002 ± 0.003	SMARTS
2991.750	5.58	3.353 ± 0.048	3.530 ± 0.054	4.540 ± 0.050	4.716 ± 0.021	0.004 ± 0.003	SMARTS
2996.750	18.98	3.505 ± 0.032	3.397 ± 0.027	4.506 ± 0.034	4.703 ± 0.017	0.005 ± 0.003	SMARTS
3013.750	6.44	3.247 ± 0.074	3.578 ± 0.099	4.480 ± 0.094	4.498 ± 0.050	-0.002 ± 0.003	SMARTS
3018.750	3.06	3.314 ± 0.049	3.613 ± 0.061	4.510 ± 0.052	4.754 ± 0.024	0.004 ± 0.003	SMARTS
3027.805	7.37	3.386 ± 0.032	3.640 ± 0.039	4.497 ± 0.037	4.740 ± 0.018	0.004 ± 0.003	SMARTS

Table 4. RXJ0911+0551 R-band Lightcurves

APPENDIX B: GLOSSARY OF TERMS

§1.1

magnitude – a logarithmic measure of an object’s brightness in a given wavelength range. Brighter objects have lower magnitudes, and a difference of five magnitudes corresponds to a factor of 100 in brightness. Mathematically, the difference between the absolute (i.e., intrinsic) magnitudes for two objects is given by

$$M_2 - M_1 = 2.5 \log \frac{L_1}{L_2}, \quad (13)$$

where L_1 and L_2 are the luminosities of the objects.

innermost stable circular orbit – this quantity can be measured in different general relativistic spacetime metrics. The Schwarzschild metric assumes a nonrotating black hole, and the radius of the innermost stable circular orbit is equal to six times the black hole’s gravitational radius $r_g = GM_{\text{BH}}/c^2$. The Kerr metric assumes a maximally rotating black hole. The corresponding orbit radius is equal to the gravitational radius r_g .

bolometric luminosity – an object’s energy output over the full electromagnetic spectrum.

inverse Compton scattering – the scattering of photons to higher energies in collisions with particles. In quasars, it is thought that the thermal radiation of the disk is “up-scattered” to X-ray energies in collisions with relativistic electrons in a surrounding hot corona.

bremsstrahlung – the “braking radiation” emitted as charged particles decelerate in interactions with other charged particles.

§1.2

angular diameter distance – a measure of distance to an object defined by the ratio of an object’s projected physical diameter to the angle it subtends on the sky. Because the universe is expanding, the angular diameter distance term contains a factor of the Hubble constant H_0 , which sets the proportionality between the distance to celestial objects and their recessional velocities along the line of sight due to the expansion of the universe. As noted in §1.3, this analysis assumed $H_0 = 70 \text{ km s}^{-1} \text{ Mpc}^{-1}$.

redshift (z) – a cosmological quantity that characterizes the distance to an object; specifically, the “cosmological redshift” is the amount by which an object’s rest-frame radiation is shifted to longer wavelengths due to the expansion of the universe. Since more distant objects are subject to faster recession in the Hubble flow (see the above discussion of h), their emitted light is more redshifted. Redshift is given by

$$1 + z = \frac{R_{\text{now}}}{R_{\text{then}}} = \frac{\lambda_{\text{observed}}}{\lambda_{\text{emitted}}}. \quad (14)$$

Here, R_{now}/R_{then} is the ratio of the current scale of the universe to its scale when light was emitted from a distant object, and $\lambda_{observed}/\lambda_{emitted}$ is the ratio of the light's wavelength as measured by the observer and its wavelength when it was emitted from the distant object.

§1.3

Hubble constant – see the entry for “angular diameter distance.”

§2

astrometry – the measurement of the positions of celestial objects. In this paper, the term simply refers to the relative positions of the lensed quasar system components in the plane of the sky.

§2.1

right ascension and **declination** – the astronomical equivalents of longitude and latitude, measured in the sky.

photometry – the measurement of the flux received from celestial objects. This project was specifically concerned with the relative fluxes of the components of the lensed quasar systems.

de Vaucouleurs profile – a commonly used empirical fit to the surface brightness observed in elliptical galaxies. It is also known as the $r^{1/4}$ law and is given by

$$\Sigma(r) = \Sigma_e \exp -7.67[(r/r_e)^{1/4} - 1], \quad (15)$$

where Σ is the surface brightness, r_e is the scale length within which half of the galaxy's total light is emitted, and Σ_e is the surface brightness at $r = r_e$.

§2.2

CCD saturation – a charge-coupled device (CCD) consists of an array of photoelectric detectors that are read out to produce digital images. Each array element has a limited capacity for photon “hits.” When this capacity is exceeded, the element is saturated and cannot provide a photon count.

cosmic rays – energetic charged particles that originate from space and enter Earth's atmosphere. Collisions with atmospheric molecules result in showers of lighter particles.

seeing – a term that refers to the blurring of images due to the distortions caused by the Earth's atmosphere. Seeing can be quantified at any given moment as the angular full width at half maximum of a point source in an exposure taken under existing atmospheric conditions.

Heliocentric Julian Day – the date in days from the frame of reference of the Sun since an initial epoch in 4713 B.C. The first three digits are typically truncated (HJD – 2450000) for clarity and to preserve computer memory when recording data.

§3.2

rest-frame effective wavelength – the wavelength at the centroid of the observing band, adjusted for cosmological redshift.

half-light radius – the scale length on the source plane within which half of the surface brightness of an object is contained.

cosmic microwave background radiation – blackbody radiation peaking at about 3 kelvin that fills the universe and is thought to be the afterglow of the Big Bang. Because the radiation is isotropic, the peculiar motion of the Sun (i.e., the motion that is not due to the Hubble flow) causes an observable dipolar Doppler shift in the background that permits a measurement of the observer’s velocity.

§4.1

F-test – a statistical test used to compare variances. Here, it is used to determine when an improvement in goodness-of-fit to lightcurve data by increasing the order of the fitting polynomial is not statistically significant.

§4.4

Eddington luminosity – the maximum radiated power at which the quasar can remain in hydrostatic equilibrium.